Università degli Studi di Padova

DIPARTIMENTO DI INGEGNERIA INDUSTRIALE

Corso di Laurea Magistrale in Ingegneria Aerospaziale

Tesi di laurea magistrale

Implementation of an actuator line method for aerodynamic analysis of horizontal axis wind turbines

Candidato:
Piana Claudio
Matricola 1128079

Relatori:
Ernesto Benini
Imran Afgan

Correlatori:
Luca Menegozzo
Andrea Dal Monte
Alistar Revell

Acknowledgement

Contents

List of Figures

List of Tables

Abstract

Day by day wind energy is getting more and more importance among renewable energies and more accurate studies on wind turbines are being considered. In this study, the NREL Phase VI turbine has been investigated using a computer code developed in C and coupled to Ansys Fluent. First the general theory has been explained and then the structure of the code has been presented. An ALM algorithm, coupled with a Blade Element Momentum (BEM) routine for the initialization of the loads, has been validated and proposed as an alternative to a full CFD analysis. In fact this method does not need to mesh the turbine geometry, without losing information about the 3D flow field. In Chapter 5 the the setup and a sensitivity analysis of the model have been performed. Different parameters have been set such as the time step and the radial distribution of loads. The grid size has also been considered as a parameter for the sensitivity analysis, both for accuracy and computation cost. Chapter 6 contains the results of the validation of the code. First the validity of using a BEM routine to initialize the loads for the ALM algorithm has been proved. In the second step of the validation, the wake flow field from ALM calculations has been compared to the one from a full CFD analysis. In Chapter 7 conclusions of the work and an overall comment to the results are exposed.

Introduction

In the last few decades wind energy applications have increased exponentially especially due to increased energy demand and to challenge global warming. So, new technologies have been developed and several studies have been conducted in order to increase the installed power. Wind power capability is among the most important renewable energies and it has been greatly financed in the last few years. Wind turbines are employed to intercept the wind flow and to convert it into mechanical and electrical energy.

Europe is seriously taking into account to grow up the production of green energy from wind. Wind energy is considered a competitive power technology and in 2017 it produced 11.6% of the energy demand in Europe. In 2017, 16.8 GW of wind power have been installed in Europe, 15.6 GW only in the European Union. 6.5 GW has been produced by Germany, followed by 2.2 GW by UK and 1.6 by France. Italy, instead, produced 252 MW for an equivalent of 1.6% of the energy produced in EU by wind turbines[1]. Offshore wind turbines have been considered more in the last years. For instance, the onshore installation has grown by 14%, while the offshore doubled and they are still increasing. Nowadays 80% of electricity has been produced by onshore turbines and 20% by offshore[1].

Renewable wind energy

In this chapter, after a brief introduction about the history of wind turbines, the global resources of wind energy are presented. Different configurations of wind turbines, then, are depicted with their advantages and disadvantages, focusing especially on the Horizontal Axis Wind Turbine (HAWT), case of interest for this thesis.

1.1 From History until Today

The first documented windmill dates back at the Persian ages (200 B.C) even if people were exploiting wind energy for other purposes. Around the 13th century the grain grinding mills started to be very popular even in Europe. The first interesting horizontal axis mill with a twisted and tapered blade was built in the land of Holland. Even if they had a crude airfoil profile, Dutch hold this record and the machine concept was imported in America. They were used especially for pumping the water to irrigate fields. A big step had been taken in Holland in 1910, when the first gear box associated with a generator was introduced, allowing the generation of energy for 20 years. For a long period, then, fossil fuels took over wind energy. Then, after the energy crisis in 70s, and particularly in the last 20 years wind turbines started to have a great influence in the energy production and they are increasing in number and in efficiency day by day.

Recently GWEC (Global Wind Energy Council) [2] has published the statistics of how the wind energy has increased during the last two decades. In the graph below it is reported the cumulative installed wind capacity from 2001 until 2017.

The tendency of using energy from wind is increasing. In fact, taking into account the climate changes and the needs of replacement of the fossil energy, it is highly probable that there will

GLOBAL CUMULATIVE INSTALLED WIND CAPACITY 2001-2017
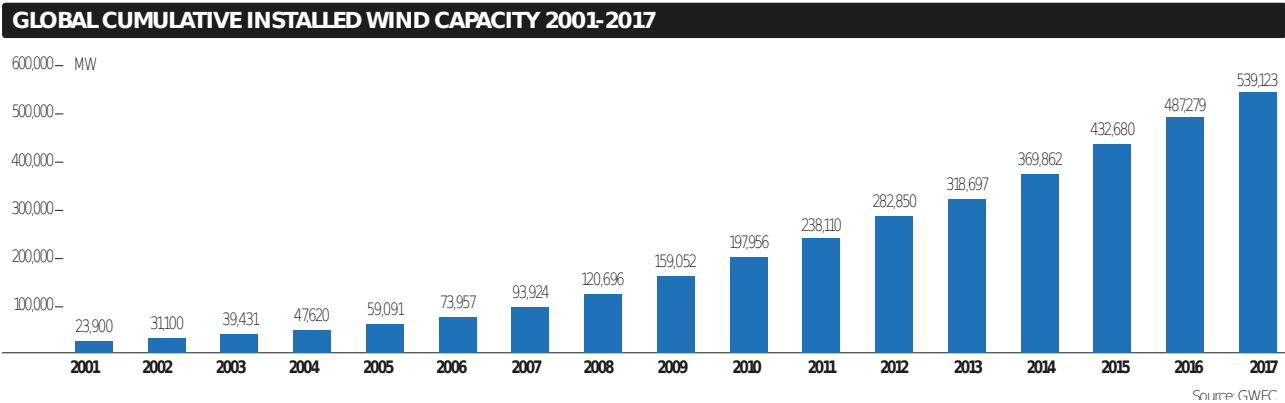
Figure 1.1: Global cumulative installed wind energy production.

be an higher investment in wind technologies.

Wind turbines, convert the wind energy firstly into mechanical energy and then into electrical energy. Wind turbines are considered to be mature and the costs of wind energy are low. So, in the last years, wind energy has gained primary importance, especially in China, USA and Germany [4].

1.2   Global energy resources and consumptions

Energy production and consumption have greatly increased over the last decades. Actually the biggest amount of energy production comes from fossil fuels. The problem is that conventional fuels increase global warming and pose people to health risk. So, it is necessary to find a valid replaceable source of energy such as renewable energies. Renewable energies will help to mitigate the climate change because they are clean and sustainable compared to fossil fuels.

1.2.1   Global Wind Energy Resources

The atmosphere is like a big heat engine. It extracts heat from the sun and transfers it to the air. So, some work is done in the gases and different pressure regions are created on Earth. The difference in air pressure causes, then, the movement of the air from a region of high pressure to a region of low pressure, which is the nature of the wind. [3]

Figure 1.2 shows the *Wind Distributions* ($\overline{x}$) on the Earth. There are some places which offer a great meteorological potential such as Greenland, the southern tip of South America, the North
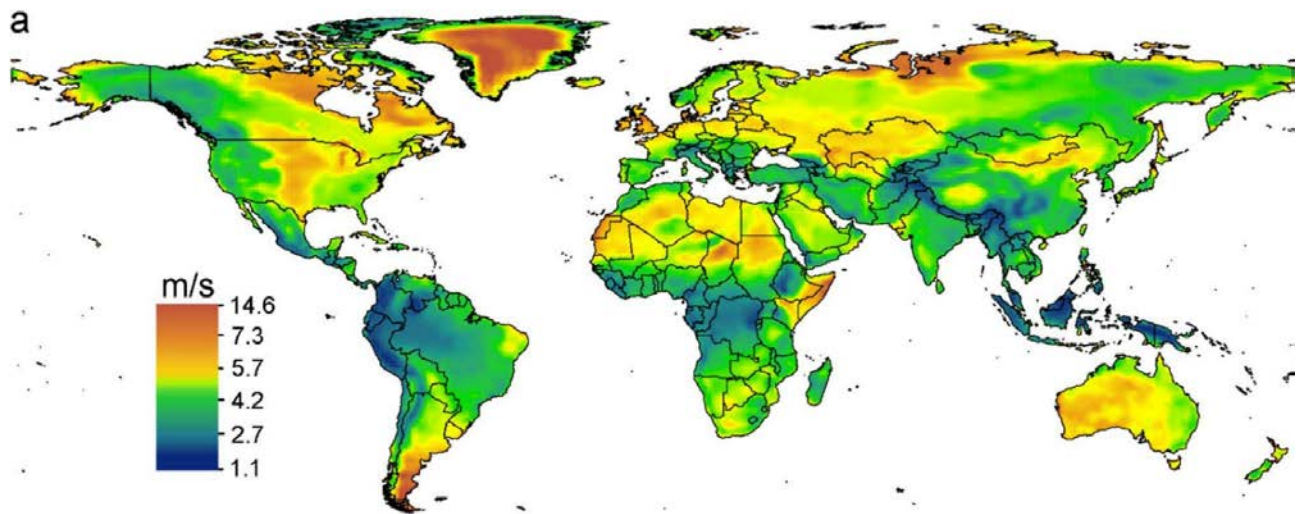
Figure 1.2: Main wind speed at 100m above ground level [4].

Sea coast, Western Sahara, Chad, Somalia, the Midwest of the USA, the north part of Canada, Russia and in the South of Australia.

Another important factor is the *Wind Power Density* ($\overline{P}$). The regions with an high $\overline{P}$ correspond to high wind distributions ($\overline{x}$). So, only the 34.1% of the lands exceed the $100W/m^2$, the lower bound for wind energy utilization. So, these areas are in general suitable for installation of wind turbines. There are some places where the actual consumption of energy is low and the presence of a small percentage of wind turbines would cover a great amount of energy request.

In a global scale some analysis shows that it would be possible to match the energy consumption if all the countries installed wind turbines at 2% in their area. A big challenge for the industrialized countries is the integration of wind energy. In fact, in those countries it is really hard to replace the existing sources of energy with new ones. On the other hand, it is easier to integrate wind energy in the developing countries. There are also some drawbacks of wind energy. The only way to make the wind turbine more competitive is to reduce the costs. In fact, the structure itself and the land where to build them are really expensive and they produce a lot of mechanical and aerodynamic noise. Noise is a really important factor especially for turbines in populated areas. Another big problem is how to convince people living close to the turbines to accept the constructions. So, to do it, companies are letting people to take part in the project and to share the income. Furthermore, noise and visual impact will be less because most of the agencies are thinking to build the turbines offshore [5].

1.3 Type of wind turbines

It is possible to classify the wind turbines according to the configuration of their rotational axis. So, in general, wind turbines are divided into *horizontal axis wind turbine* and the *vertical axis wind turbines*.

HAWT   VAWT - Savonius   VAWT - Darrieus
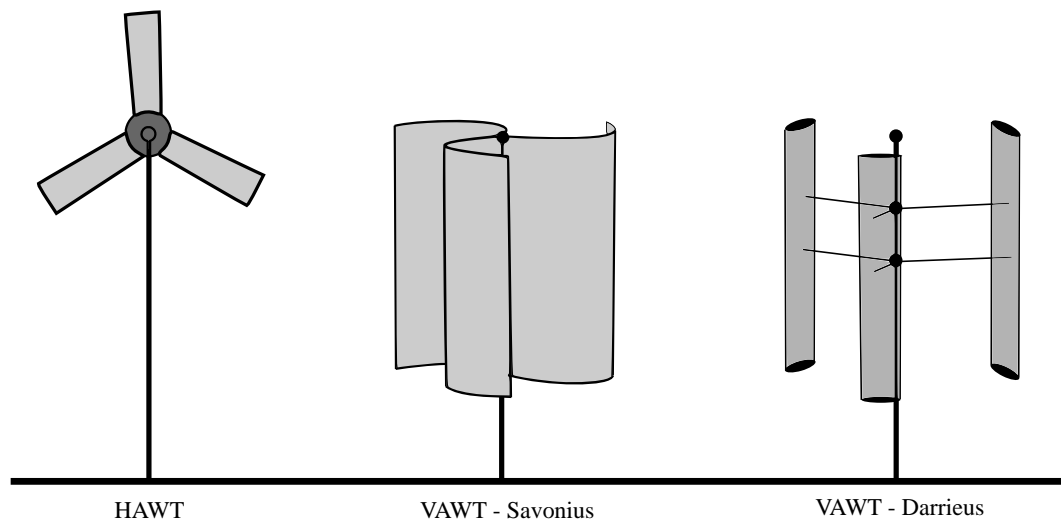
Figure 1.3: Different kind of wind turbines.

The ***Horizontal axis wind turbines (HAWT)*** are the most common wind turbines. This kind of turbines then is similar to the concept design of a windmill. The main rotor shaft and the electrical generator are located at the top of the tower and they are directed into the wind. Moreover for small turbines it is just necessary to locate a simple wind vane to move the turbine in the direction of the wind, while a wind sensor combined to a servo-motor is set for big turbines. The rotor in general is placed in front of the tower, so the wind firstly encounters the rotor and then the tower: this allows to avoid turbulences on the blades. Some *advantages* [6] for HAWTs are

- The tower, which allows the access to a stronger, wind;

- The direction of the wind is always positive for the airfoils, which compose the blades during the whole rotation (in contrast with VAWTs).

There are also some *disadvantages* [6], indeed, due to:

- The massive tower construction for the support of the blades, the gearbox and the generator;

- The assembly of the wind turbine;

- The height of the structure can be an obstacle for the landscapes and sometimes it can find the opposition of people;

- HAWTs require also an additional mechanism for the control of the yaw system, necessary to rotate the rotor into the direction of the wind;

- HAWTs in general requires also a braking system to avoid high speed rotation, which can destroy or damage the turbine.

A ***Vertical axis wind turbine (VAWT)*** has the main rotor shaft arranged vertically. A characteristic of this turbine is that it is not necessary to point the rotor into the wind. This is really useful when there is a large variation of turbulence or a quick change in wind direction. With a vertical axis, furthermore, it is possible to place the generator on the floor and consequently to operate the maintenance more easily. A great *advantage* of using VAWTs is that no yaw mechanism is needed. They also have a really low start-up speed. The main *disadvantage* is that this kind of turbine has a lower efficiency than a HAWT due to the additional drag. Moreover they are located closed to the ground, so they cannot take the advantage of the high speed above.
Other type of VAWTs are ***Savonius*** and ***Darrieus*** turbines. The first ones produce a lot of vibrations, which decrease their structural reliability. In general, then, those turbines need an extra power supplement to start rotating, from an induction motor used also to brake if the rotation speed is too high. The second ones are drag turbines, so, they are less efficient compared to HAWT.

1.4   Horizontal axis wind turbines

The wind encountering the blades produces the rotor rotation, which is connected to the low speed shaft. There are two kind of horizontal axis wind turbines:

- Upwind: wind first encounters the rotor and then it flows around the nacelle. The control system is placed after the rotor;

- Downwind: more rare compared to the upwind. The wind first encounters the nacelle and then the rotor. The control system is before the rotor.
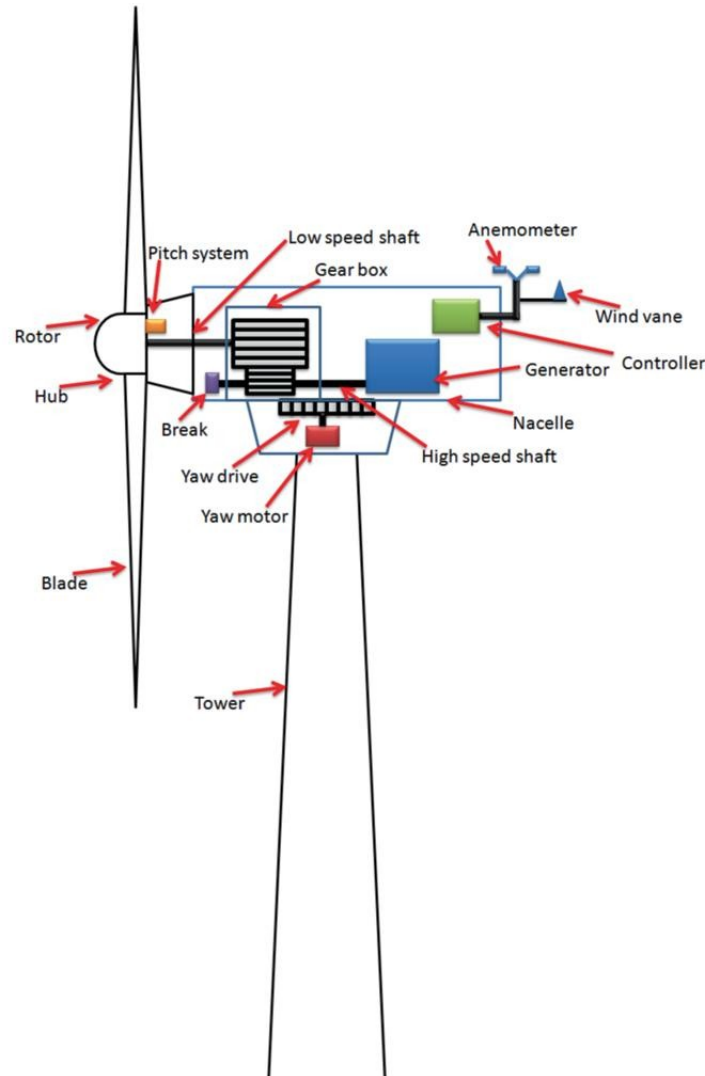
Figure 1.4: Main components of an Horizontal axis wind turbine.

The purpose of the ***nacelle*** is to support some components, such as the generator, the drivetrain and the control system. The rotor rotation caused by the wind is converted into electric energy inside the nacelle. The *drivetrain* is a series of mechanical components, such as gears, bearing and shafts. So, in the *gearbox* the low speed shaft, which is supporting the bladed system, encounters the high speed shaft with a transmission ratio that can reach 100 times.

Currently turbines are using ***pitch-controlled variable generators***, so this means that the pitch angle is changing according to the wind direction. At the hub, then, there is a system of bearings,

which allow the blades to pitch. Furthermore, the angle of attack can be optimized, so the blade can produce the maximum lift for a fixed wind velocity without stalling. The blades have a really important role in the conversion of the kinetic energy into mechanical energy. So, blades are built using airfoils specifically designed for wind turbine applications, which direct the wind force into the low speed shaft. The airfoils of the turbine influence the streamlines of the airflow. This produces a difference in pressure which leads to the lift and drag components around the airfoil. A torque moment is generated as consequence, so, in this way, the rotor rotates. Lift and the Drag depends on some parameters, in particular the shape of the blades, the surface area, the wind speed and the angle of attack. Experience, then, shows that the best number of blades for the maximum efficiency is three.

The *pitch system* is very important for the overall efficiency. A controller decides how much a blade should turn considering the optimization of the attack angle and the relative velocity seen by the blade.

The attack angle is, of course, function of the incoming wind, so there is just an optimal attack angle for a specified wind velocity. The *blade*, in fact, is *twisted* considering the designed incoming wind.

For different incoming velocities the blade would work not at its maximum efficiency. Modern concepts include also smart-blade design in which each blade is divided into several segments provided with their own pitching servomotor system.

The *main shaft (low-speed shaft)*, then, has both the functions to support the rotor and to transfer the torque moment to the gearbox and the generator. The main shaft drives the high speed shaft. The main function of the *gearbox* is to match the low speed shaft with the high speed shaft. The rotor of a wind turbine is rotating slow, so, normally, a rotor is rotating at 20 rpm and the gearbox increase the rotational speed by about 90 times. The high speed shaft is then connected to the generator.

The main electrical part is the *generator*, which produces alternating current.

A way to optimize the wind turbine operation is to use the *control system*. The main purpose of the control system is to increase the power production setting the yaw system, the blade pitch and the generator. The system is made of computers, which monitor continuously the situation of the rotor and process the data coming from the sensors. There are different kind of sensors. The most important calculate the wind features, like the anemometer, which measures the wind,
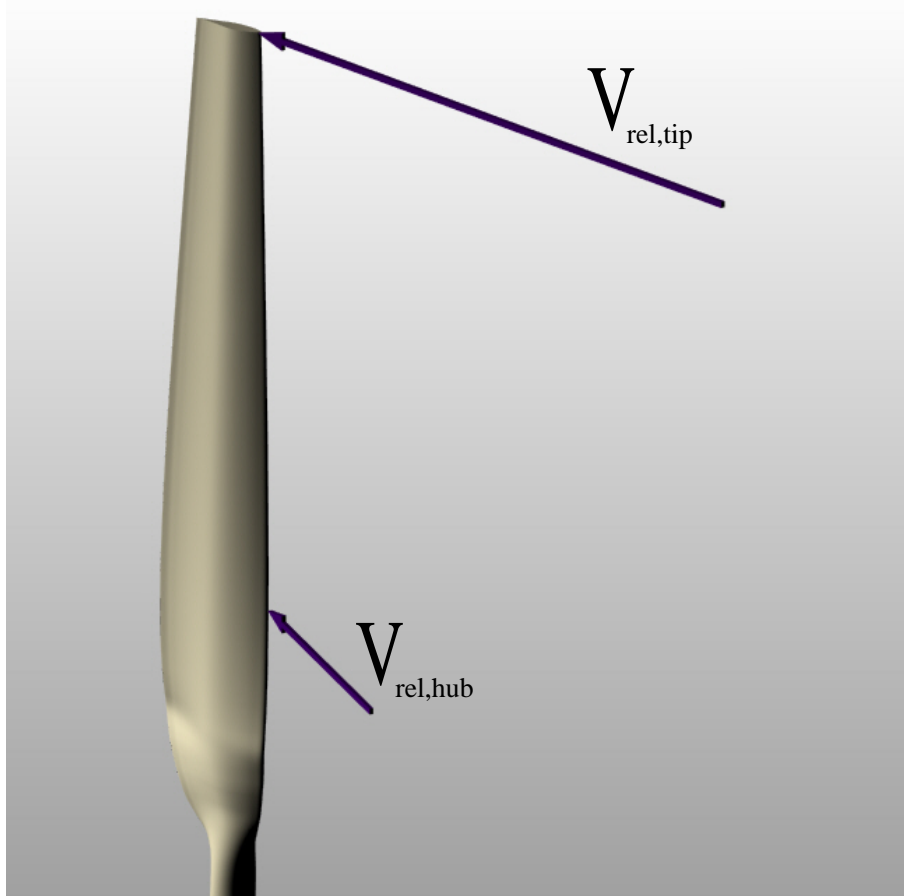
Figure 1.5: The concept of twisted blade.

speed and the LIDAR that can detect some information of the wind even a little far from the
rotor. Other sensors are measuring the rotational speed of the turbine, the temperatures of wind,
oil and of the gearbox bearing, the pitch angle and the intensity of the nacelle vibrations.
Modern turbines apply an active yaw control to get the best performances. The controller then
is adjusting also the pitch angle of the blades to tune the attack angle according to the speed of
the wind. The controller is also setting the limits in rotational speed. When the wind velocity is
usually over 25 m/s the system does not allow the increasing rotation speed of the rotor to avoid
excessive aerodynamic loads and when the wind is fewer than 3-5 m/s the system is keeping
the rotor rotating. The system, then, can operate mechanically, electrically or hydraulically
according to the design of the structure. [7]

CHAPTER 2

Mathematical Background

In this chapter all the mathematics involved in the model is described. A quick description on how a CFD problem can be set and what equations are exploited on this kind of analysis is exposes. At the end, the Linear Momentum Theory, the Blade Elements Method (BEM) and the Actuator Line Model (ALM), are described.

The *Computational Fluid Dynamics (**CFD**)* is a method, which solves fluid dynamics problems through computer calculations. Nowadays, CFD has a great importance in the industrial design and in academic research. The main *advantages* of such a methodology is the reduced cost compared with the experimental tests, the possibility to analyse the system under critical conditions and to get some results in the area of interested.

The CFD analysis is mainly divided in three parts:

- *Pre-Processing*: in this process, the geometry, the mesh, the fluid model and boundary conditions are defined. This step is crucial to determine the accuracy and the computational time need to get the results. The mesh has a great influence on the results and, because of this, it is important to investigate the mesh with a sensitivity's test to get a good compromise between computational time and accuracy;

- *Solving*: in this process the fluid dynamic equations are solved exploiting through the Finite Volume Method. So, the equations of the flow motion are integrated for each Control Volume of the domain, switching the problem into a system of algebraic equations, which can be easily solved by iterative methods;

- *Post-Processing*: in this part of the process, the results are extracted and interpreted.

2.1   Equations leading the CFD analysis

In this section the equations which solve the fluid domain are represented. There are three main equations to be considered. The *Mass Conservation Equation*, the *Momentum Conservation Equations* and the *Conservation of Energy*. by solving those equations it is possible to describe how the fluid is flowing. So, considering an infinitesimal control volume dV, the equation of conservation of mass, or continuity equation, can be written as follows:

$$\frac{\partial \rho}{\partial t} + \nabla \cdot (\rho \boldsymbol{U}) = 0 \tag{2.1}$$

where ρ is the density of the fluid and U velocity vector. This equation is valid both for compressible and for incompressible flows, but for the second case, it reduced to:

$$\nabla \cdot \boldsymbol{U} = 0$$

The *Momentum Conservation Equation* considers the sum of the forces acting on the elements as shown on the following equation:

$$\frac{\partial \rho \boldsymbol{U}}{\partial t} + \nabla \cdot (\rho \boldsymbol{U} \boldsymbol{U}) = -\nabla p + \nabla \cdot \bar{\bar{\tau}} + \rho \boldsymbol{g} + \boldsymbol{f} \tag{2.2}$$

where f is the sum of the body forces acting on a element, $\bar{\bar{\tau}}$ is the tensor of stress defined in [8] as:

$$\bar{\bar{\tau}} = 2\mu s_{ij} + \lambda \delta_{ij} \nabla \cdot \boldsymbol{U} \qquad s_{ij} = \begin{cases} \dfrac{\partial u_i}{\partial x_i} \\ \dfrac{1}{2}\left(\dfrac{\partial u_i}{\partial x_j} - \dfrac{\partial u_j}{\partial x_i}\right) \end{cases}$$

with δ_{ij} *Kronecker delta*.

The third equation is the *Energy Conservation Equation* which is defined as:

$$\rho \frac{\partial E}{\partial t} + \rho \nabla \cdot (\rho E \boldsymbol{U}) = -\nabla \cdot (p\boldsymbol{U}) + \nabla \cdot (\bar{\bar{\tau}} \cdot \boldsymbol{u}) + \nabla \cdot (k\nabla T) + S_E \tag{2.3}$$

where:

- $q = k\nabla T$ is the rate of heat transfer as defined by the Fourier law.

- S_E is the energy source term;

- E is the sum of internal and kinetic energy.

In this work an incompressible flow has been considered, so the *Energy Conservation Equation forse* is not considered. In this way *Ansys-Fluent* uses some specific algorithms for combining pressure with velocity, such as *SIMPLE*, *SIMPLEC* or *PISO*.

Defined an i-th variable ϕ_i as the sum of the time-averaged valued and its fluctuation as:

$$\phi = \bar{\phi}_i + \phi_i'$$ (2.4)

it is possible to find the averaged value as:

$$\bar{\phi}_i = \frac{1}{\Delta t} \int_{t_0}^{t_0 + \Delta t} \phi_i dt$$ (2.5)

Appling all those considerations on the all variables of the Navier-Strokes equation, the *Reynolds Averaged Navier-Stokes equations (RANS)* can be computed. So, exploiting those equations, the computational time is reduced without losing accuracy in the results.

2.2   Linear Momentum Theory for an Ideal Wind Turbine

The one-dimensional model is important to set the basic theory of wind turbine aerodynamics. A wind turbine extracts energy from wind, converting it into mechanical energy. For the linear momentum theory, the rotor is modelled as a one dimensional permeable disc. The disc, is considered ideal, so there is no friction and there are no rotational velocity components in the wake. The disc is slowing down the wind from V_0, of the undisturbed incoming flow, to u at the rotor plane and to u_1 in the wake. The drag is calculated by the pressure drop Δp over the rotor. The one dimensional momentum equations are useful to derive some important relations.

Now, consider a constant axial velocity u passing through the disc of area A and a constant axial load, or thrust. In the ultimate wake, the pressure reaches the undisturbed conditions (p_0). ρ is the density and consider A_0 and A_1 as the areas at the upstream and the downstream of the rotor as shown in the Figure 2.1. The mass flow rate through the disc is given by:
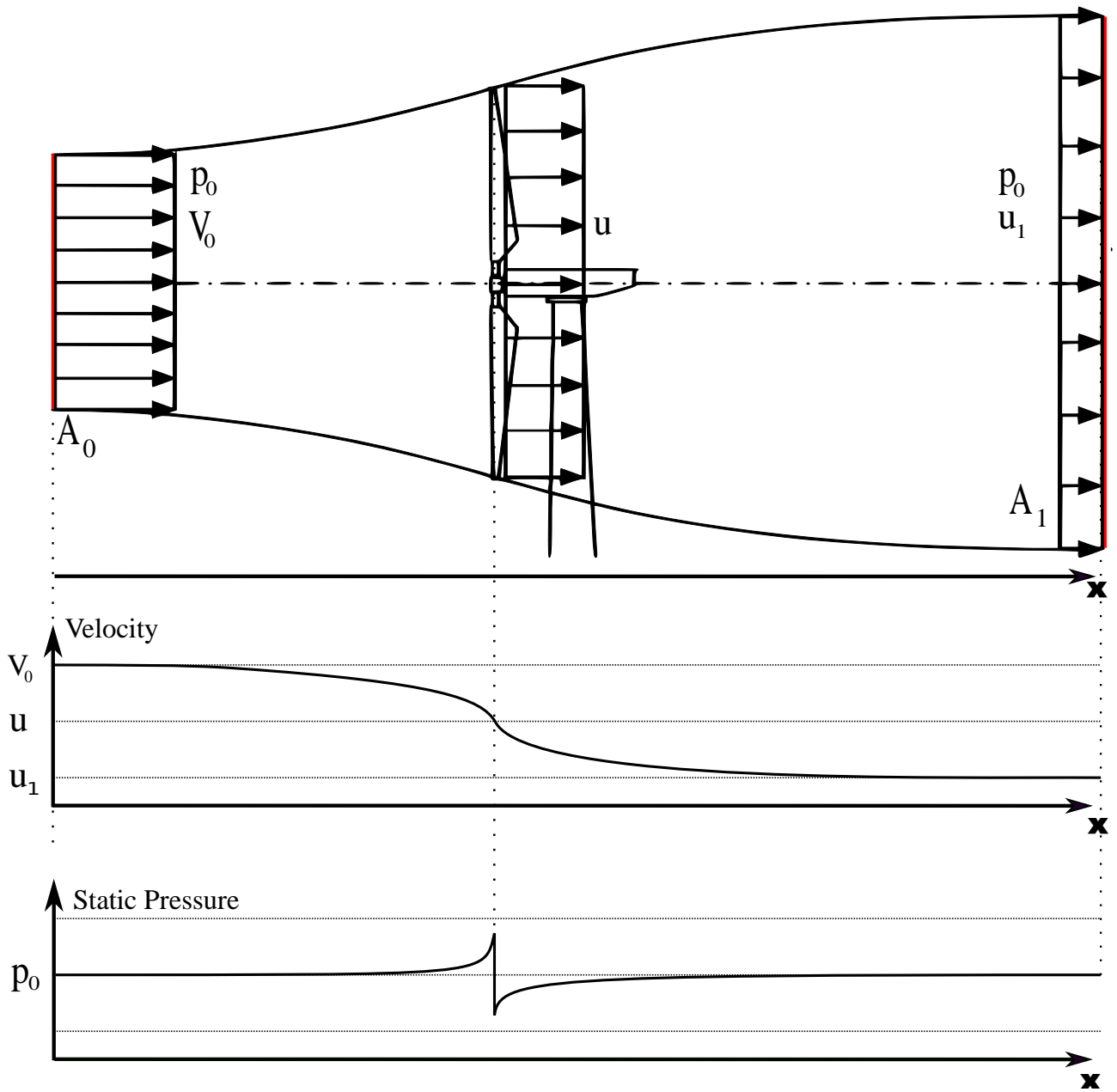
Figure 2.1: Illustration of some streamlines passing through the rotor, the axial velocity and the pressure upstream and downstream the rotor.

$$\dot{m} = \int \rho u \, dA = \rho V_0 A_0 = \rho u A = \rho u_1 A_1 \qquad (2.6)$$

which gives also a relationship between the upstream and the downstream variables. The axial momentum balance, instead, is calculated by:

$$T = \dot{m}(V_0 - u_1) = \rho u A(V_0 - u) \qquad (2.7)$$

The basic assumptions are that the lateral pressures is neglected and that the pressure in the wake and in the upstream are the same. Applying the Bernoulli's equations, it is easy to extract the pressure gap across the disc:

$$p_0 + \frac{1}{2}\rho V_0^2 = p + \frac{1}{2}\rho u^2 \qquad\qquad p + \frac{1}{2}\rho u^2 = p_1 + \frac{1}{2}\rho u_1^2$$

$$\Delta p = \frac{1}{2}\rho(V_0^2 - u_1^2) \tag{2.8}$$

The thrust then can be calculated as $T = A\Delta p$. So, combining the equation 2.7 and 2.8, the velocity in the rotor disc is equal to:

$$u = \frac{1}{2}(u_1 + V_0) \tag{2.9}$$

Introducing now the axial induction factor:

$$a = \frac{V_0 - u}{V_0} \tag{2.10}$$

we get the following velocities in function of the axial factor:

$$u = (1 - a)V_0 \tag{2.11}$$

$$u_1 = (1 - 2a)V_0 \tag{2.12}$$

Substituting the 2.11 and the 2.12 into the thrust and power equations, we get:

$$T = 2\rho V_0^2 a(1 - a)A \tag{2.13}$$

$$P = 2\rho V_0^3 a(1 - a)^2 A \tag{2.14}$$

Once calculated the power and the thrust, the following parameters can be extracted:

$$C_P = \frac{P}{\frac{1}{2}\rho A V_0^3} \tag{2.15}$$

$$C_T = \frac{T}{\frac{1}{2}\rho A V_0^2} \tag{2.16}$$

Substituting the previous Equations 2.15 and 2.16 into 2.14 and 2.13, it is possible the get two
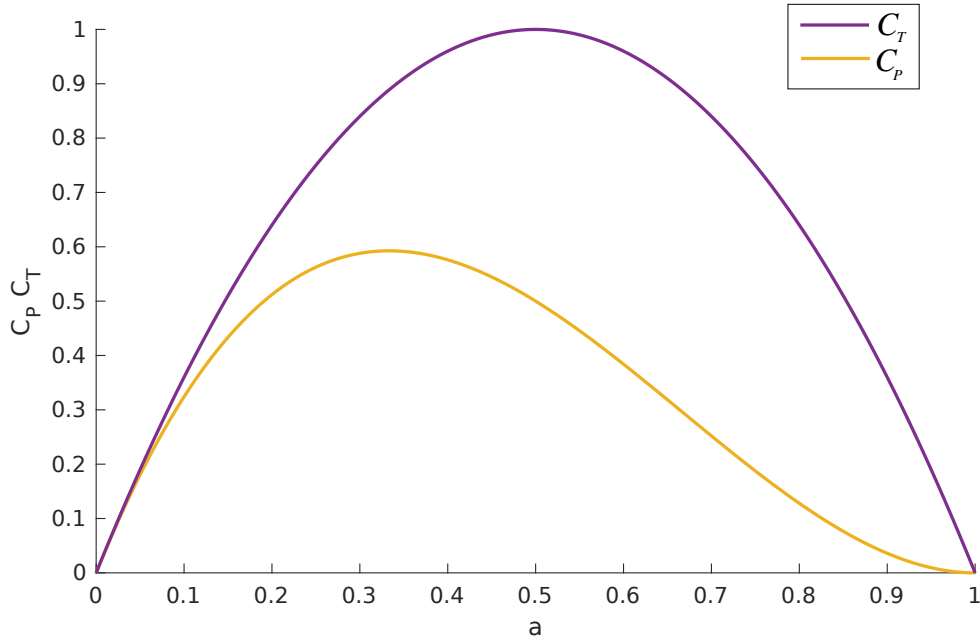
Figure 2.2: The power and the thrust coefficients as function of the axial induction. For a less then 0.5 this theory is valid.

equations for the ideal one dimensional wind turbine:

$$C_P = 4a(1 - a)^2 \tag{2.17}$$

$$C_T = 4a(1 - a) \tag{2.18}$$

Differentiating the C_P, yields:

$$\frac{dC_P}{da} = 4(1 - a)(1 - 3a) \tag{2.19}$$

$a = 1/3$ gives $C_{p,max} = 16/27$. The Equations 2.17 an 2.18 are plotted in Figure 2.2. The maximum power coefficient is well known as *Betz limit*.

The momentum theory is not valid for values higher then 0.5 because, as it is obvious from the Equation 2.12, the wake velocity would be negative. So, from values of a, grater then 0.33, the Glauert empirical relation is used. The main reason for which the momentum theory is not valid for a greater then 0.33 is that the shear layer at the edge of the wake becomes unstable when the gap between the velocities $V_o - u_1$ is really high. So, eddies are formed for high difference in velocity from the outer to the inner flow. This condition is called *turbulent wake state* [10]. Moreover a better explanation of the corrections is shown in the Section 2.3.

2.2.1 Effects of rotation

Considering an ideal rotor, the tangential induction factor a' is zero. If applied to an infinitesimal control volume of thickness dr along the disc, the power becomes:

$$dP = \dot{m}\omega r C_\theta$$

$$= 2\pi r^2 \rho u \omega C_\theta dr \tag{2.20}$$

Where C_θ is the azimuthal component of the absolute velocity. The force applied to the blades of the turbine is in equilibrium with the one experienced by incoming air, but in the opposite direction. In the Figure 2.3 it is shown that the $V_{rel,1}$ is given by the sum of the vectors V_{rot} and the incoming wind speed u.
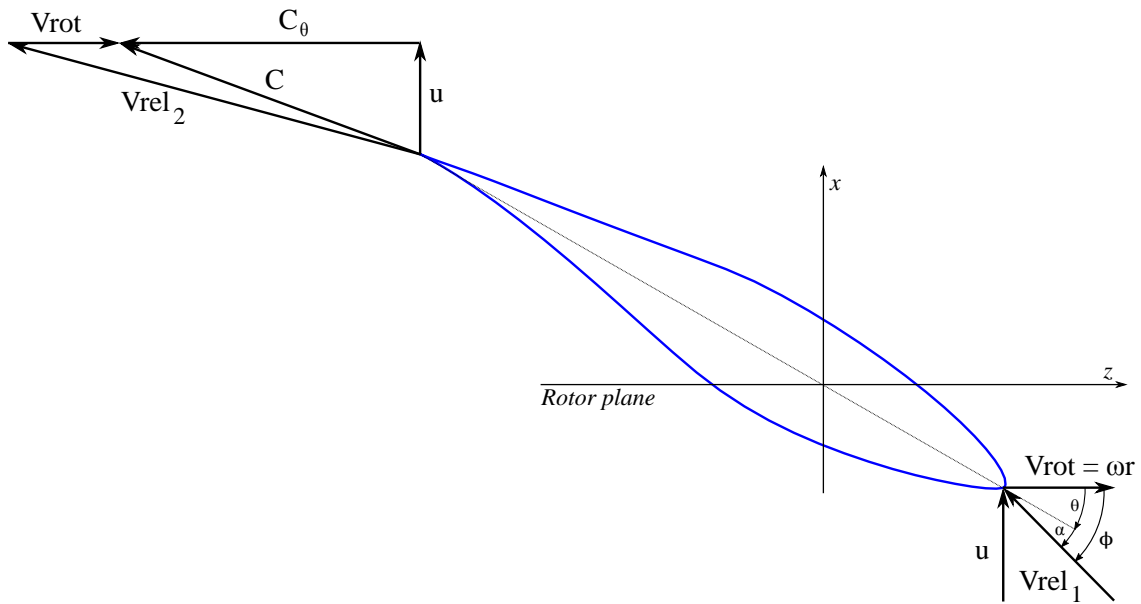
Figure 2.3: The triangle velocities for a specific section of the rotor.

For low angles of attack at the leading edge of the rotor, at the trailing edge $V_{rel,2}$ is almost following the trailing edge. The axial component remains the same for the conservation of the mass and the rotational speed is the same. The velocity triangle on the downstream shows that C, the absolute velocity of air, is the sum of C_θ, in opposite direction of Vrot, and u. Recalling

31

the definition of the axial induction factor, it is also possible to define the rotational speed of in the wake in function of the *tangential induction factor a'* as follows:

$$C_\theta = 2a'\omega r \tag{2.21}$$

So, substituting inside equation 2.20 and reminding Equation 2.11:

$$dP = 4\pi\rho\omega^2 V_0 a'(1-a)r^3 dr \tag{2.22}$$

And the *Total Power* is given by integration from the center of rotation to the tip from 0 to R:

$$P = 4\pi\rho\omega^2 V_0 \int_0^R a'(1-a)r^3 dr \tag{2.23}$$

The power coefficient, introducing the Tip speed ratio λ and the local speed ratio λ_r is given by:

$$C_p = \frac{8}{\lambda^2} \int_0^\lambda a'(1-a)\lambda_r^3 d\lambda_r \tag{2.24}$$

where λ is the *tip ratio speed* $\lambda = \omega R/V_o$ and λ_r is the local rotational speed $\lambda_r = \omega r/V_0$. From the Equation 2.23 and 2.24 it is clear that a condition to optimize the power is to maximize the $a'(1-a)$ term in the integral. It is possible to extract the relationship between the axial and the tangential induction factor, which becomes:

$$a' = \frac{1-3a}{4a-1} \tag{2.25}$$

2.3 Blade Element Momentum Method

In this section the classical Blade Element Method model is explained [11]. Applying this method it is possible to calculate the steady loads and also thrust and power for different value of wind speed, rotational speed and pitch angle. The method follows the 1-D momentum theory described before and considering the local 2D aerodynamics around the airfoil. A stream tube is discretized into N annular elements of height dr, as can be seen in Figure 2.4.

In the BEM it is assumed that:

- Steady state flow;

- Frictionless surfaces;

Rotor Plane

Control Volume

R

r

dr
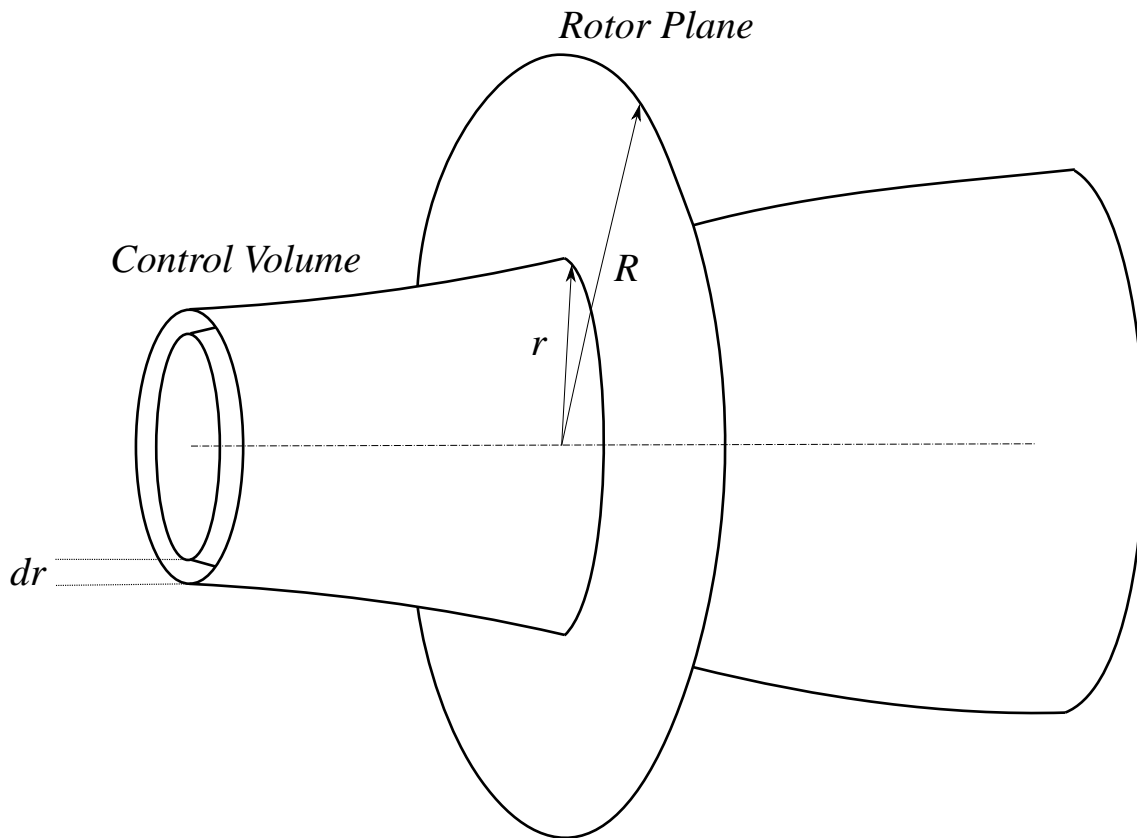
Figure 2.4: The concept of discretization into N annular elements of height dr.

- No radial dependency between each layer of the blade;

- No radial flow across the elements;

- The force from the blades on the flow is constant in each annular element, this means infinite number of blades.

The thrust from each control volume can be found using the following formula:

$$dT = (V_0 - u_1)d\dot{m} \tag{2.26}$$

$$= 2\pi r \rho u(V_0 - u_1)dr \tag{2.27}$$

Where $2\pi r\,dr$ is the annular sector. The torque acting on each annular element, using the integral

moment of the momentum equation, is given by:

$$dM = rC_\theta d\dot{m}$$

$$= 2\pi r^2 \rho u C_\theta dr \qquad (2.28)$$

From the 1D momentum theory it is well known that the axial velocity in the wake is in function of V_0 and the axial induction factor. So, introducing Equation 2.11, Equation 2.12 and Equation 2.21 into Equation 2.27 and 2.28, the Equation for the torque and moment in the annular section of the disc is computed as:

$$dT = 4\pi r \rho V_0^2 a(1 - a)dr \qquad (2.29)$$

$$dM = 4\pi r^3 \rho V_0(1 - a)a'dr \qquad (2.30)$$

The relative velocity is the combination of the axial and tangential velocity and it is possible to see it in Figure 2.5.

θ is the angle between the chord line and the rotor plane and it is the combination of the tip pitch angle θ_{tip} and the twist angle β:

$$\theta = \theta_{tip} + \beta$$

ϕ, flow angle, is the angle between the rotor plane and the relative velocity to the airfoil. The angle of attack is then calculated as:

$$\alpha = \phi - \theta \qquad (2.31)$$

where ϕ is derived from:

$$\tan \phi = \frac{(1 - a)V_o}{(1 + a')\omega r} \qquad (2.32)$$

It is now important to remember that the lift is perpendicular to the direction of the wind and the drag is parallel to that direction as sketched in Figure 2.6. So, lift and drag per spanwise length are calculated as:

$$L = 0.5\rho V_r^2 c C_l \qquad (2.33)$$

$$D = 0.5\rho V_r^2 c C_d \qquad (2.34)$$
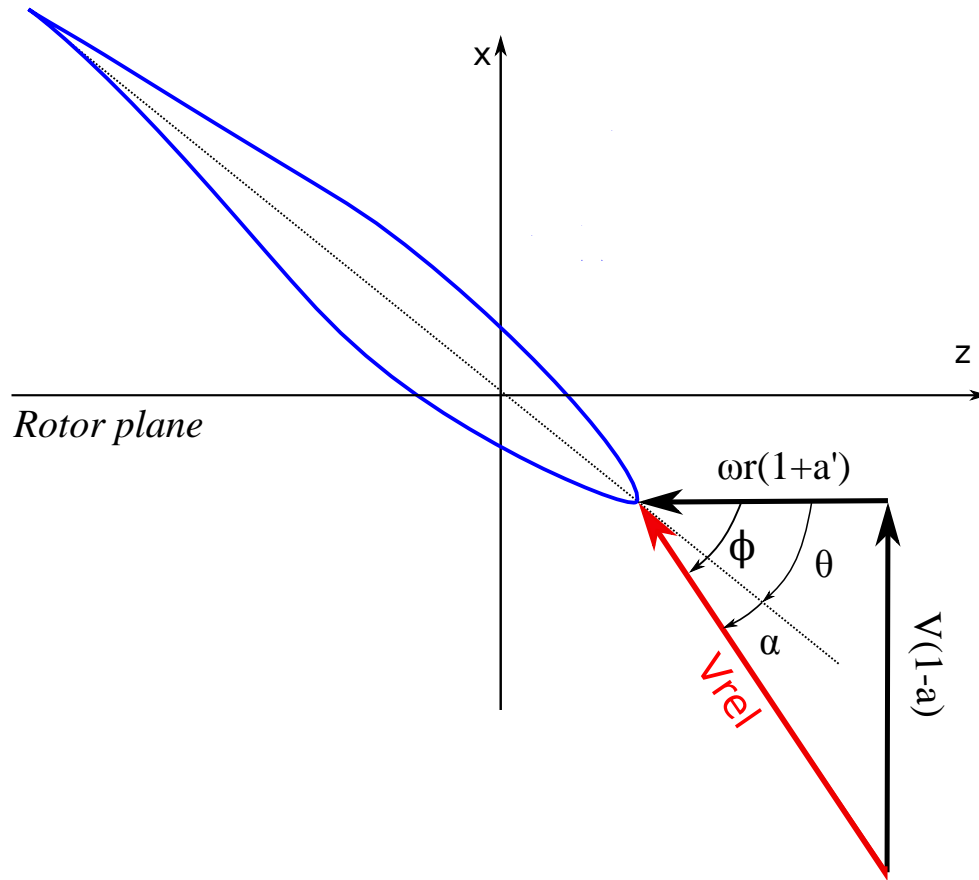
Figure 2.5: Velocity triangle in a general section of the blade.

Those forces can be projected into the plane containing the airfoil as:

$$p_n = L \cos \phi + D \sin \phi \tag{2.35}$$

$$p_t = L \sin \phi - D \cos \phi \tag{2.36}$$

From the p_n and p_t it is possible to deduce the following dimensionless coefficients:

$$C_n = C_l \cos \phi + C_d \sin \phi \tag{2.37}$$

$$= \frac{p_n}{0.5 \rho V_r^2 c} \tag{2.38}$$

$$C_t = C_l \sin \phi - C_d \cos \phi \tag{2.39}$$

$$= \frac{p_t}{0.5 \rho V_r^2 c} \tag{2.40}$$
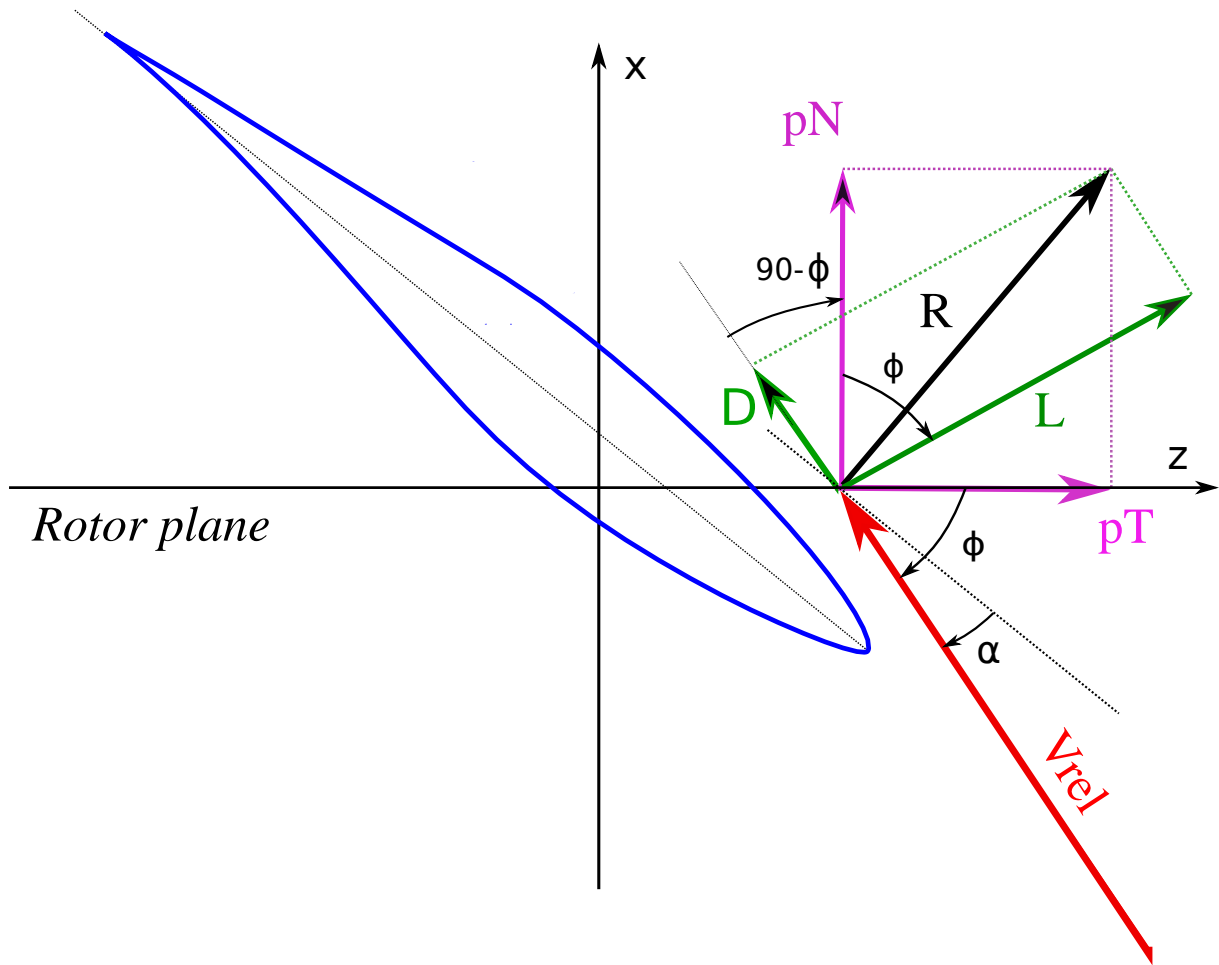
Figure 2.6: Local Lift and Drag divided into normal and tangential components to the rotor-plane.

Moreover from the Figure 2.5 is easy to find the following relations:

$$V_r \sin \phi = V_0(1 - a) \tag{2.41}$$

$$V_r \cos \phi = \omega r(1 + a') \tag{2.42}$$

Another factor σ, solidity, is defined for each annular area in the control volume:

$$\sigma(r) = \frac{c(r)B}{2\pi r} \tag{2.43}$$

Where B is the number of the blades, $c(r)$ is the local chord and r is the radial position of the control volume. Since p_n and p_t are forces per unit length, it is immediate to perform the thrust

and the moment as follow:

$$dT = Bp_n dr \tag{2.44}$$

$$dM = rBp_T dr \tag{2.45}$$

Now, substituting Equation 2.41 for V_r into Equation 2.38 and using Equation 2.38 for p_N into Equation 2.44, we obtain:

$$dT = \frac{1}{2}\rho B \frac{V_o^2(1-a)^2}{\sin^2 \phi} cC_n dr \tag{2.46}$$

Now, substituting Equation 2.41 and 2.42 for V_r into Equation 2.40 and using Equation 2.40 for p_T into Equation 2.45, the result is:

$$dM = \frac{1}{2}\rho B \frac{V_o(1-a)\omega r(1+a')}{\sin \phi \cos \phi} cC_t r dr \tag{2.47}$$

Combining the Equation 2.46 with Equation 2.29 the axial induction factor becomes:

$$a = \frac{1}{\dfrac{4\sin^2 \phi}{\sigma C_n} + 1} \tag{2.48}$$

Combining the Equation 2.47 and Equation 2.30, the tangential induction factors becomes:

$$a' = \frac{1}{\dfrac{4\sin \phi \cos \phi}{\sigma C_t} - 1} \tag{2.49}$$

Now it is possible to iteratively compute the forces acting on the rotor. So, for each radial layer the solution can be treated separately and it can be extracted iteratively as:

a) Initialize a and a', usually to 0;

b) Compute the flow angle ϕ using equation 2.32;

c) Compute the local angle of attack using equation 2.31;

d) Read the values of $C_l(\alpha, Re)$ and $C_d(\alpha, Re)$ from the polar tables;

e) Compute C_n and C_t from Equations 2.37 and 2.39;

f) Calculate the induction factors from Equations 2.48 and 2.49;

g) If the values differ from the ones of the previous iteration more than a certain tolerance, go to b) or else finish;

h) Compute the local loads on the segment of the blade.

To get a general view of the problem it is important to consider the **Prandtl's Tip Loss Factor** and the **Glauert Correction** for high values of a. In fact the 2D polar tables does not considers the 3D losses. The Prandtl tip-loss correction defined by Equation 2.51 is included in the calculation of the axial induction factor as:

$$a = \frac{1}{\dfrac{4F \sin^2 \phi}{\sigma C_n} + 1} \tag{2.50}$$

where

$$f_{TL} = \frac{2}{\pi} \cos^{-1} F \qquad F = \frac{N}{2} \frac{R_{tip} - r}{r \sin \phi} \tag{2.51}$$

If the axial induction factor is greater than 0.4, the simple momentum theory starts to break down. In order to get better results, it is appropriate to consider the Glauert correction:

$$\begin{cases} a = \dfrac{1}{\dfrac{4F \sin^2 \phi}{\sigma C_n} + 1} & if \ a_c < 0.2 \\ a = \dfrac{1}{2}[2 + K(1 - a_c) - \sqrt{(K(1 - 2a_c) + 2)^2 + 4(Ka_c^2 - 1)}] & if \ a_c > 0.2 \end{cases}$$

where

$$K = \frac{4F \sin^2 \phi}{\sigma C_n}$$

The Glauert theory consider the finite number of blades, so, it has been necessary to upgrade this correction in order to fit better the real case. In [13], in order to consider the three dimensional tip losses, the following corrections are applied to the normal and tangential coefficients:

$$Cn = F_1 C_n^{2d} \tag{2.52}$$

$$Ct = F_1 C_t^{2d} \tag{2.53}$$

where C_n^{2d} and C_t^{2d} are the projections along the rotation axis of the lift and drag coefficient from the 2D airfoil. The correction F_1 is defined as follows:

$$F_1 = \frac{2}{\pi} \cos^{-1} \left[\exp \left(- g \frac{B(R - r)}{2r \sin \phi} \right) \right] \tag{2.54}$$

where g depends on the tip speed ratio, the chord and the number of blades. g is represented in the following equation:

$$g = \exp \left[- 0.125(B\omega R_{tip}/V_{inlet} - 21) \right] + 0.1 \tag{2.55}$$

Consequently, the axial and tangential induction factors can be computed as in [13]:

$$a = \frac{2 + Y_1 - \sqrt{4Y_1(1 - F) + Y_1}}{2(1 + FY1)} \tag{2.56}$$

$$a' = \frac{1}{((1 - aF)Y_2/(1 - a)) - 1} \tag{2.57}$$

where F is the tip loss coefficient losses as in 2.51 and Y_1 and Y_2 are defined as:

$$Y_1 = \frac{4F \sin^2 \phi}{\sigma C_n^{2d} F_1} \tag{2.58}$$

$$Y_2 = \frac{4F \sin^2 \phi \cos^2 \phi}{\sigma C_t^{2d} F_1} \tag{2.59}$$

2.4   Actuator line method

The actuator line method, introduced by Sørensen and Shen, is a three-dimensional method for the unsteady aerodynamic model of the wind field. The actuator line method shows some interesting characteristics which give a lot of *advantages*, such as:

- The Actuator Line Model does not need a large usage of elements, because it does not show the boundary layer's problem since the blade geometry in not modelled the fluid domain;

- It is possible a detailed investigation of the wakes and of the eddies behind the turbine;

- The mesh can be easily built.

There are also some *disadvantages*:

- Some parameters need to be set (such as parameter ϵ) and there is not a standard method to follow;

- It is necessary to import the tables of lift and drag depending on the Reynolds number which are an approximation of the real coefficients.

The method combines the equation of Navier-Stokes with the actuator line technique. The blades are divided into N elements (Figures 2.8 and2.7) and represented in the fluid domain as forces radially distributed in the spanwise direction. An equivalent force is then applied in correspondence of each element.
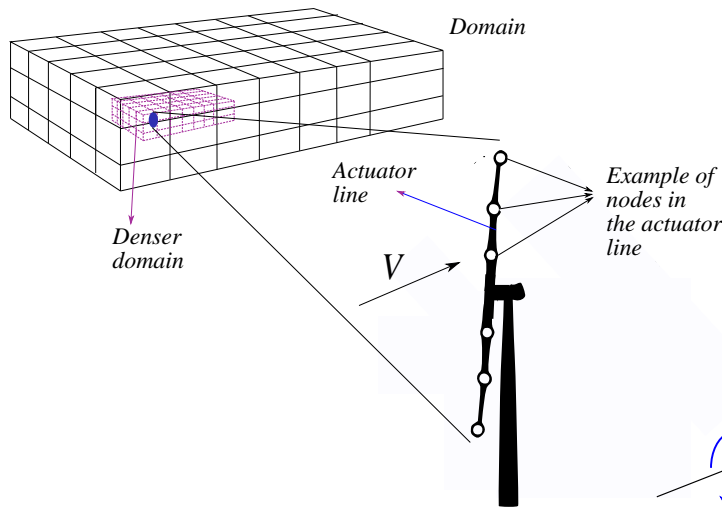
Figure 2.7: Domain and concept of the actuator line.   **Figure 2.8:** Segmentation of a blade.
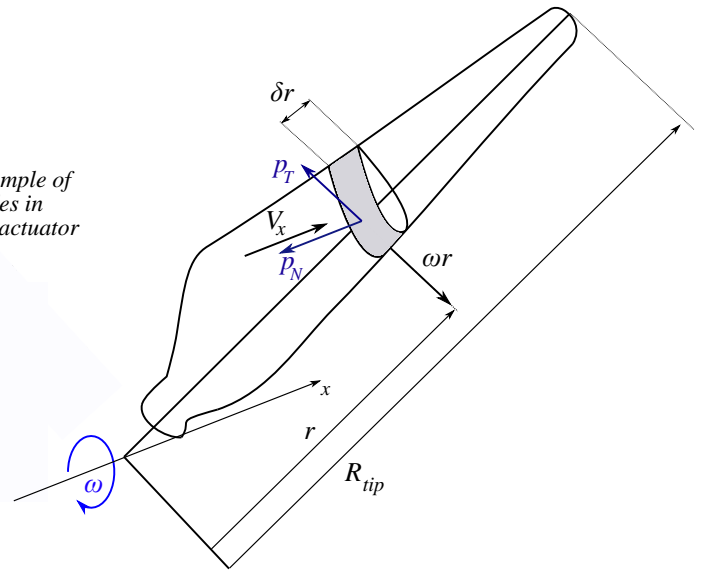
First, the geometry of the blade described by its chord and twist is imported as table and interpolated for each section. Lift and drag coefficients depending of both the attack angle and the Reynolds number can be extracted and interpolated. Once computed the velocity variables it is possible to compute the forces using the Equations 2.33 and 2.34. Then, after projecting the force along the main axis of the domain (Equations 2.35 and 2.36), the f term for the incompressible Navier-Strokes equation

$$\frac{\partial \vec{V}}{\partial t} + \vec{V} \cdot \nabla \vec{V} = -\frac{1}{\rho}\nabla p + \nu \nabla^2 \vec{V} + \vec{f} \tag{2.60}$$

$$\nabla V = 0 \tag{2.61}$$

is well known and it can be added as body force on the fluid domain in the actuator points. The Figure 2.3 shows an example of airfoil in the (x,z) plane, where the direction of the lift and drag forces and the velocities at the leading edge are represented. Thus, representing the velocity triangle, the local relative velocity at each blade element can be calculated as shown in the Figure 2.5. Finally, using the flow angle and the axial induction factor, the relative velocity can be computed as follow:

$$V_{rel} = \frac{V_0(1-a)}{\sin \phi} \tag{2.62}$$

The flow angle between the relative velocity and the rotor plane is given by Equation 2.32 from the BEM theory; the attack angle, then, is just the difference between the flow angle and the sum of the global pitch angle and the twist angle discussed in the Section 2.3. Having the knowledge of the attack angle, the airfoil table can be imported and interpolated to get the 2D lift and drag coefficients. Since the BEM theory has been validated, the relative velocity computed can be used for the calculation of the lift and the drag forces leading a 2D airfoil and it can be computed as in the Equations:

$$\vec{L} = 0.5\rho V_{rel}^2 c C_l \vec{e}_L \tag{2.63}$$

$$\vec{D} = 0.5\rho V_{rel}^2 c C_d \vec{e}_D \tag{2.64}$$

where $\vec{e}_L$ and $\vec{e}_D$ are respectively the Lift and Drag directions. Multiplying the equations by the spanwise length Δr, the lift and drag forces, leading to a segment, can be calculated.

Another important factor is the *regularization kernel*, which permits the forces along the actuator line to be smoothed out using a three dimensional Gaussian distribution. This is necessary since the forces, divided by the volume of the cell, are too large to avoid singularity problems. This can be obtained, as shown in [14], by the convolution between the forces and the regularization kernel, as follow:

$$\vec{f_\epsilon} = \vec{f} \otimes \mu_\epsilon \tag{2.65}$$

$$\mu_\epsilon(d) = \frac{1}{\epsilon^2 \pi^{3/2}} \exp\left[-\left(\frac{d}{\epsilon}\right)^2\right] \tag{2.66}$$

where $d = |\vec{x} - s\vec{e}_i|$ is the distance between the centroid of the cell in the domain and the considered i-th point in the actuator line. $\vec{e}_i$ are the unit directions and ϵ is the smooth parameter

which is used for the load's regularisation. The regularized force per unit volume becomes:

$$\vec{f_\epsilon}(x) = \sum_{i=1}^{B} \int_{0}^{R} \vec{f_{2D}}(s)\mu|\vec{x} - s\vec{e_i}|ds \tag{2.67}$$

In this section the actuator line method has been described; the code, coupled with Ansys Fluent, will be later discuss in Chapter 4.

CHAPTER 3

Numerical Setup

In this chapter, the wind turbine model, adopted for the validation of the code, is presented and its specification illustrated. In particular, the first section shows the characteristics of the NREL PHASE VI wind turbine and an example of the extended airfoil table. The next sections describe, first the solver and then, the set up of the model and finally conclude with depicting the boundary conditions cases applied in the simulations.

Nowadays in the world, an higher and higher demand of energy is growing. However people are also decided to focus on renewable energies such as wind energy. The development of the wind energy, one of the most important types of renewable energies, has taken hold in the last decades. Researchers studied different airfoil configurations for a better aerodynamic and, hence, a better efficiency. In this way, NREL PHASE VI, which has S809 foil, represents a good example of high wind technology.

In order to obtain accurate results of the ALM, the BEM model first at all has to be validated with the experimental data. The table for the geometry and experimental data have been extracted from [15].

3.1   Specification of NREL Phase VI wind turbine

The NREL Phase VI wind turbine, developed by The National Wind Technology Center at the National Renewable Energy Laboratory, has been extensively tested, thus it is characterized by a complete experimental database. That is why it is a common benchmark in wind turbine code validations, and it has been considered also in this research.

The standard blade NREL Phase VI wind turbine has the features shown in the Table 3.1.

Table 3.1: Main parameters of the NREL PHASE VI turbine.

Number of blades	2
Hub Height	12.20 m
Rotation Speed	71.86 rpm
Rotor Radius	5.029 m
Rotation direction	CCW
Orientation	upwind
Rotor hub	25% of Rotor radius
Yaw	0°
Global Pitch angle	5°
Nominal Power	19.80 KW
Cut in Speed	6 m/s
Airfoil	S809

The blade shows a tapered and twisted configuration. The chord and twist trends are represented in the Figures 3.1 and 3.2. The pitch angle then is kept constant with a null cone angle.
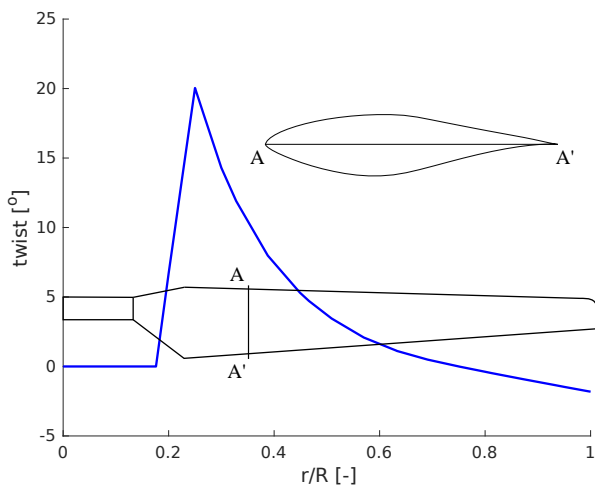
Figure 3.1: The twist angle distribution.
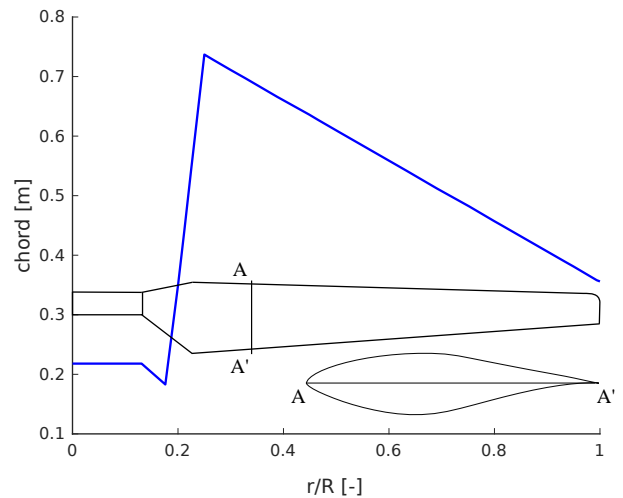
Figure 3.2: The chord distribution.

Since the R_{hub} is starting at 25% of the blade, this method is not considers the nacelle, compromising a little bit the results. Moreover, the table of lift and drag coefficients are evaluated from RFOIL, which has an higher accuracy of the coefficients in the stall conditions. Then, by importing the airfoil profile it was possible to extract its tables in function of the Reynolds number. Since RFOIL produce data only for a small range of attack angle, the NWTC

[1] provides a script to extend the airfoil table to a larger angle of attack, getting a complete control and a good approximation in 360°. In Figure 3.3 it is shown the trend of the extended lift and drag coefficients if function of the attack angle for Re=1.6E6 while in Figure 3.4, the experimental data are represented in function of inlet velocity from 7.016 to 25.109 m/s.

3.2 Mesh Configuration

The computational domain has been built up directly from *Pointwise 18.1* and exported in *.cas*, ready to be imported in ANSYS-FLUENT. The grid domain is composed of 4.8 millions hexahedral structured cells, for the purpose to take advantaged with a solution strategy in the calculations which will be discussed in the Section 3.5. The turbine's center has (0,0,0) coordinates both for the Absolute and the Relative (rotating with the rotor) system frames. The relatives system has a counter clockwise rotation such as the turbine. The computational domain measures 16R x 16R x 24R and most of the cells has been concentrated in the turbine's region (4R x 4R x 3R) where R and is the turbine radius and they assume the volume of 0.004 m^3. Moreover 4.8 million elements are just enough for the validation of the turbine, while for a wake analysis a big amount of cells should be added.

Pointwise, then, let the author to initialize the solvers, hence, the 3D-ANSYS-FLUENT has been selected. The inlet, the outlet and the symmetry boundary conditions has been attributed to their respective surfaces of the domain and the fluid region to the volume inside the boundaries.

Another important check as to be considered for the distance of the boundary surfaces. In fact, if the fluid domain is too short along the direction of the fluid, the flow does not have space enough, in the fluid domain, to stabilize and to reach the convergence leading the simulation to swing.

The lateral boundary conditions then have also to be far enough to let the air to enlarge behind the turbine. If this last condition is not respected, in fact, the flow can not freely distribute in the radial direction, leading the flow to accelerate in the fluid field around the momentum sources, affecting the results (see Section 5.3).

---

[1]https://www.nrel.gov/nwtc/
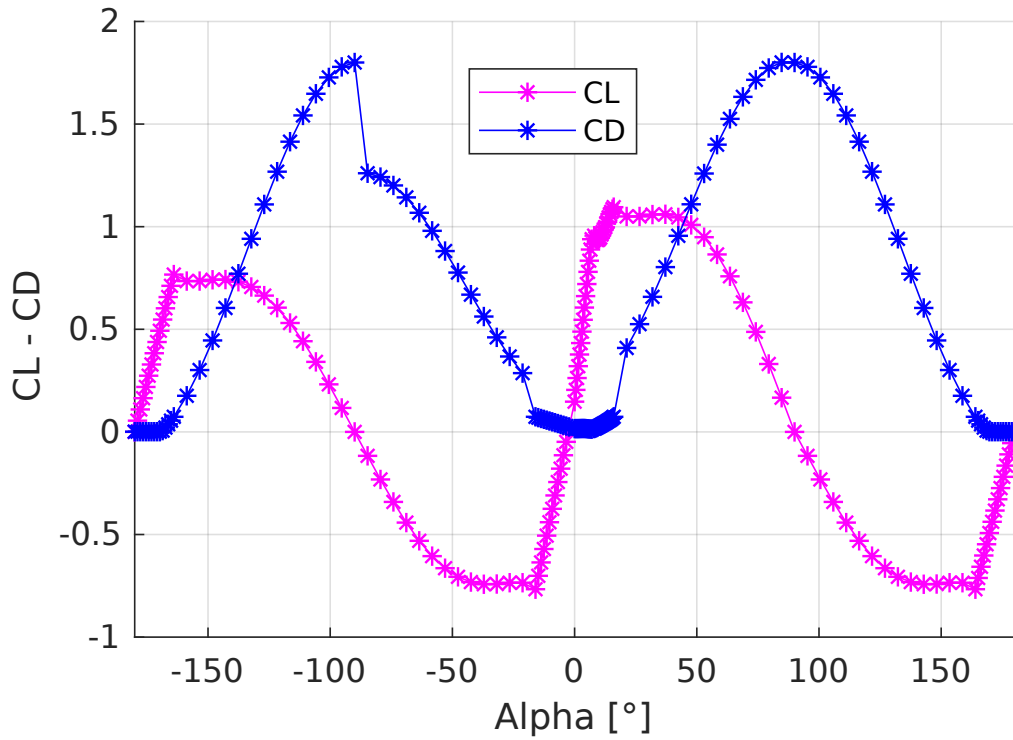
Figure 3.3: Example of CL and CD extended coefficients for the S809 airfoil profile at Re=1.6E6.
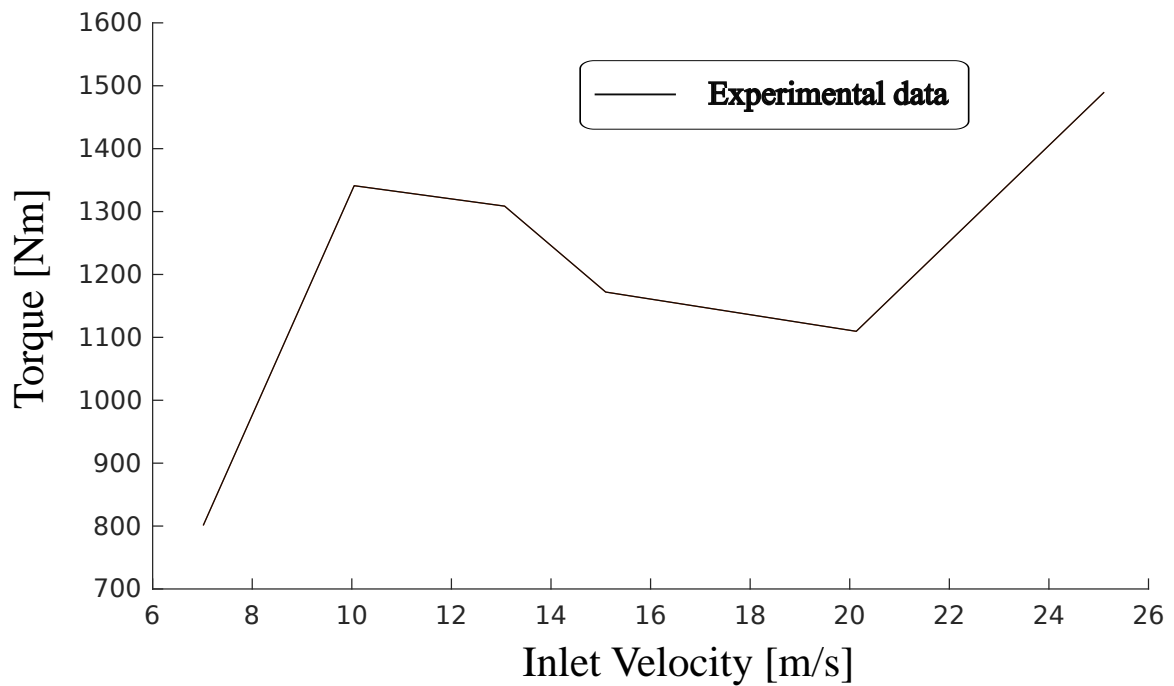
Figure 3.4: Representation of the experimental torque.
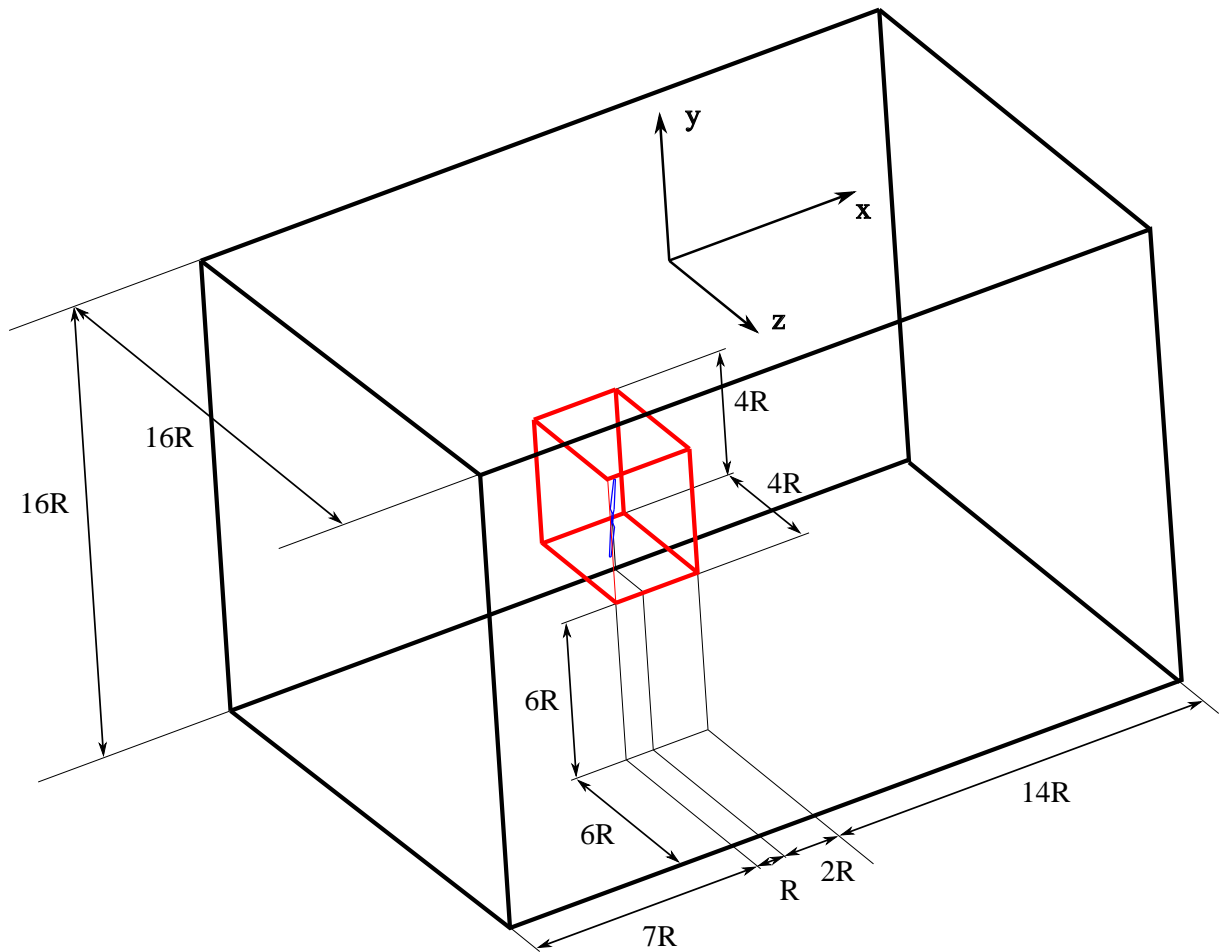
Figure 3.5: Representation of the domain. The red box underlines the volume where the turbine is set and where most of the cells are concentrated. R is the rotor radius.

3.3 Solver Setup and Boundary Conditions

The computational mesh has been imported in the ANSYS-FLUENT 16.1 pre-processor, one of the most common CFD software adopted both in academic and industrial fields. The implementation of the actuator line and the inlet boundary conditions are built up through some User Defined Functions (UDF) in C-programming. For all the simulations, the density of the fluid has been set incompressible for all the simulations. ANSYS-FLUENT, moreover, uses the *Finite Volume Method (FVM)* and the solution for a general problem is reached by the following steps:

- Integration of the fluid-dynamic equations into a finite on a finite system of control

volumes;

- Transformation of integral equations into algebraic equations (discretization);

- Solve the equation using iterative methods.

The boundary conditions used are reported on the Table 3.2:

Table 3.2: Boundary conditions.

Inlet b.c.	Velocity inlet
Outlet b.c.	Pressure outlet
Lateral surfaces b.c.	Symmetry

where the *inlet velocity* define the direction and the magnitude and the direction of the fluid. The UDF for the inlet velocity will be described in the Section 4.1. The *pressure outlet* is defined as normal to the fluid outlet surface and is set to 0, far enough to have the condition of far-field. The *symmetry* conditions are set around the fluid domain and they show a null shear stress on the surfaces, for the purpose to neglect frictions which can be found in other conditions (such as wall conditions). Air material has been attributed at the domain fluid in pressure-based conditions with constant density at 1.246 kg/m^3 and dynamic viscosity 1.769e-5 Pa s.

3.4 Turbulence model

In this work the fluid domain is simulates using a transient approach (URANS) with the $k - \varepsilon$ standard turbulence model. Since there are no boundary layers on the domains, this method represent the best solution for this case setup. It was also considered to use the $k - \omega$ *SST* model, but the weak point is the sensitivity of the solutions to values for k and ω outside the shear layer (freestream sensitivity). While the new formulation implemented in ANSYS Fluent has reduced this dependency, it can still have a significant effect on the solution, especially for free shear flows teAnsysFluent0. So, the $k - \varepsilon$ *standard* used is a two-equations model which is computationally lighter then other models and more evaluated for a fully turbulent domain. The additional equations taken into account refers to the transport equations of the turbulent kinetic

energy k and the dissipation rate ε:

$$\frac{\partial}{\partial t}(\rho k) + \frac{\partial}{\partial x_i}(\rho k u_i) = \frac{\partial}{\partial x_j}\left[\left(\mu + \frac{\mu_t}{\sigma_k}\right)\frac{\partial k}{\partial x_j}\right] + G_k + G_b - \rho\varepsilon - Y_M + S_k \quad (3.1)$$

$$\frac{\partial}{\partial t}(\rho\varepsilon) + \frac{\partial}{\partial x_i}(\rho\varepsilon u_i) = \frac{\partial}{\partial x_j}\left[\left(\mu + \frac{\mu_t}{\sigma_\varepsilon}\right)\frac{\partial\varepsilon}{\partial x_j}\right] + C_{1\varepsilon}\frac{\varepsilon}{k}(G_k + C_{3\varepsilon}G_b) - C_{2\varepsilon}\rho\frac{\varepsilon^2}{k} + S_\varepsilon$$

$$(3.2)$$

In these equations, G_k represents the generation of turbulence kinetic energy due to the mean velocity gradients. G_b is the generation of turbulence kinetic energy due to buoyancy. Y_M represents the contribution of the fluctuating dilatation in compressible turbulence to the overall dissipation rate. $C_{1\varepsilon}$, $C_{2\varepsilon}$ and $C_{3\varepsilon}$ are constants, while σ_k and σ_ε are the turbulent Prandtl numbers for k and ε, respectively. S_k and S_ε are user-defined source terms [17].

The eddy viscosity (μ_t) in then calculated combining the transport equations:

$$\mu_t = \rho C_\mu \frac{k^2}{\varepsilon} \quad (3.3)$$

where C_μ is a constant.

For a deeper description of the model and a good explanation of the constants considered before, please consider the [16] and [17].

3.5 Coupling Pressure-Velocity (PISO)

As far as it is known there is no equation coupling the pressure-velocity, as said in the Section 2.1. The *Pressure-Implicit with Splitting of Operators (PISO)* pressure-velocity coupling scheme, part of the SIMPLE algorithms, hence represent the best choice to solve this problem. The PISO algorithm, in this way, improves the coupling between the pressure and the velocity by performing two additional corrections: the neighbour correction and skewness correction [18]. Since the mesh is structured in the way that both the upstream and the downstream can be clearly identified, the *QUICK* scheme is used for extract an higher-order of ϕ, the convected variable, at a face. For example at the face e in the Figure 3.6, the one dimensional control volume, for the flow from left to right, the variable ϕ can be written as:

$$\phi_e = \theta\left[\frac{S_d}{S_c + S_d}\phi_P + \frac{S_c}{S_c + S_d}\phi_E\right] + (1-\theta)\left[\frac{S_u + 2S_c}{S_u + S_c}\phi_P - \frac{S_c}{S_u + S_c}\phi_W\right] \quad (3.4)$$
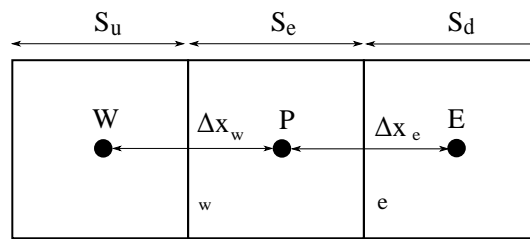
Figure 3.6: Representation of the QUICK scheme.

It is possible to split up this formula into three main cases:

1. $\theta = 0$ is the *second order upwind* value;

2. $\theta = 1/8$ represents the *QUICK scheme*, the case of interest;

3. $\theta = 1$ is the *central second order interpolation*.

It is also important to remember that this method is more efficient when the mesh is aligned with the flow direction. If the mesh is not aligned the other methods will be automatically switched on [19]. In this study, the *Bounded Second Order Implicit Time Integration* is also used for a better stabilization of the unsteady variables.

CHAPTER 4

Code Description

In this chapter the code has been development and structure are described. A brief description of the implementation of the BEM is described in the first section, while a representation of the macros used by the ALM algorithm described and the logic of the algorithm implemented in Ansys-Fluent with a C-code is explained in details.

4.1 Code structure

To develop the ALM code, some UDFs (User Defined Functions) are used to personalize the ANSYS-FLUENT standard libraries. The UDFs, written in C-programming, allow to increase the versatility of the software, to study complex configurations, and to add sources to the pre-set equations governing the fluids dynamics. The momentum equation, in this specific case, has been updated by the addition of the momentum sources as shown in the Equation 2.2. The code is divided into two main blocks:

1. A BEM routine. The spanwise aerodynamic forces computed by the BEM model are used as input in the Ansys-Fluent solver and to initialize the ALM algorithm.

2. The ALM algorithm itself. The radial forces computed by BEM are imposed to a series of points, rotating inside the 3D fluid domain, in order to model the presence of the rotor without meshing its geometry.

The purpose to match the two models is to simulate the model without geometry which has less cells, is faster and has no boundary layers. Hence, BEM is crucial to give an initialization to the ALM. The general structure of the code is reported in Figure 4.1. The UDFs are macro defined
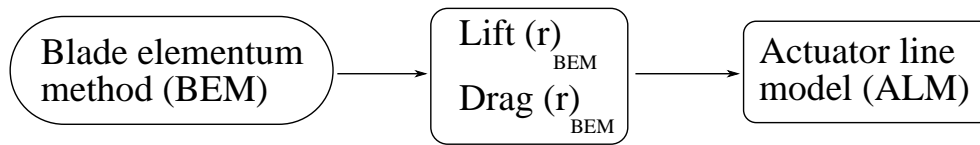
51

Figure 4.1: Representation of the general functionality of the code.

in the ANSYS-FLUENT database which can be recalled and compiled into the software. The algorithm needs the following UDFs:

- `DEFINE_EXECUTE_ON_LOADING` in which the polar tables of interest has been imported;

- `DEFINE_ADJUST`, where the main code has been developed;

- `DEFINE_PROFILE` which applies a velocity profile to the domain inlet;

- `DEFINE_SOURCE`, which imposes the momentum sources in the flow domain;

- `DEFINE_EXECUTE_AT_END` which is used to print variables at the end of each time step.

4.1.1 Development of the BEM initializer

The `DEFINE_EXECUTE_ON_LOADING` is a general macro which is executed when UDF library is loaded. In this case some tables have been imported in order to be available during the simulation. The tables imported in this macro are listed below:

- The twist and chord table, represented in Figures 3.1 and 3.2 which are interpolated along the radius;

- The values of the velocity inlet 7.016, 10.047, 13.069, 15.098, 20.131 and 25.109 m/s to validate the standalone BEM module comparing the experimental data of torque with the computed value;

- Four extended polar tables, as shown in the Figure 3.3 of the lift and drag coefficients variable with the attack angle and of the Reynolds number. The four tables refer to 4 different values of the Reynolds number, respectively at 0.4e6, 1e6, 1.6e6 and 2e6 which are interpolated in the main macro once the attack angle is computed. As explained in

the previous Section 3.1, the tables are extracted from RFOIL and extended using Viterna method from -180 to 180 degree.

The BEM routine is inside the DEFINE_ADJUST macro. The BEM algorithm can initialize the ALM. In fact:

a) The velocities computed by the BEM routine in the rotor plane, reduced by the induction factors, are used for the calculation of the Lift and Drag forces;

b) Lift and Drag forces, calculated by the BEM routine for each radial position, are the input for the ALM algorithm.

The DEFINE_PROFILE is a macro used to set the velocity inlet in the fluid domain. The begin_f_loop is a macro which loops over the faces in all the domain. The F_PROFILE macro, once hooked in the software, defines the new inlet velocity value assigned and it is declared as global variable to be recall in every line of the code.

4.1.2   Development of the ALM algorithm

The ALM method has been developed into the DEFINE_ADJUST macro. First at all, the begin_c_loop has been used to loop all over the cells. In the first c loop, the C_R(c,t) and the C_VOLUME(c,t) respectively the density and the volume of each cell are extracted from the flow field and imported to the code. Then, the position of the actuator points is calculated with al loop over the cells:

```
#define N 26          /*Actuator points along one blade*/
#define B 2           /*Number blades*/
for (p=0; p<N; p++){  /*Loop over actuator points*/
for (n=0; n<B; n++){  /*Loop over the blades*/
/*In here it is computed the:
1) Location of the actuator points along the blades;
2) New position of the actuator line*/
thread_loop_c(t,d)
{
begin_c_loop
/* Minimum distance calculation*/
...
...
```

So, discretized the blade into N segments from R_{hub} until R_{tip} and assigned the respective actuator points, with the proper momentum source from the BEM initialization, and the initial position of the blades, the actuator line, which represents the blade itself, is ready to start rotating. So, since the transient analysis considers the time dependence, the macros `CURRENT_TIMESTEP` and `N_TIME` can be used to determine the rotation angle of the rotor at each time step as follows:

$$rot_{ang} = \omega N_{t_s} \Delta t \tag{4.1}$$

where N_{t_s} is the number of time steps adopted in the simulation, ω is the rotation speed in the counter clockwise direction, if the rotor is seen from upwind, and Δt is the size of the time step. This concept of the rotating actuator line is represented in Figure 4.2. To have a more clear reference, it is defined a new system frame (x',y',z') rotating with the rotor. Through a rotation matrix ($R_x(rot_{ang})$) along the rotation axis of the turbine, the new coordinates of the actuator points at each time step can be computed.

In order to calculate the coordinates of the nearest cell to the location of the actuator point, the loop over the cells, this time, is exploited to solve a minimum problem. The `C_CENTROID(cent,c,t)` macro provides the coordinates of the cell centroid. So, calculating the distance between the actuator points and the centroid coordinates (Figure 4.2) of the cells, it is possible to extract the minimum distance and to choose the desired cells where to apply the momentum forces. The second blade is modelled by locating the actuator points 180 degree after the first blade.

Now, taking advantages of the BEM initialization, the forces can be computed and they can be imported in Ansys-Fluent. Since Ansys-Fluent requires the source terms in generation rate per unit volume the computed forces have to be divided by the volume of each cell which is imported through the `C_VOLUME(c,t)` macro.

Since the volumes are small, the equivalent forces calculated are high and the software can suffer of singularity. A solution to this problem is represented in Figure 4.3, which shows the Gaussian distribution cantered at each actuator point and distributed around a spherical volume. First of all, the Gaussian distribution function have to be normalized considering the distance between the actuator points and the coordinates of the centroids of the cells in the spherical volume and secondly convoluted with the force computed in the code to be smeared in the spherical volume. After the projection of all the forces in the 3 inertial directions, the actuator lines are ready to be imported in the software and to be imposed in the flow field.
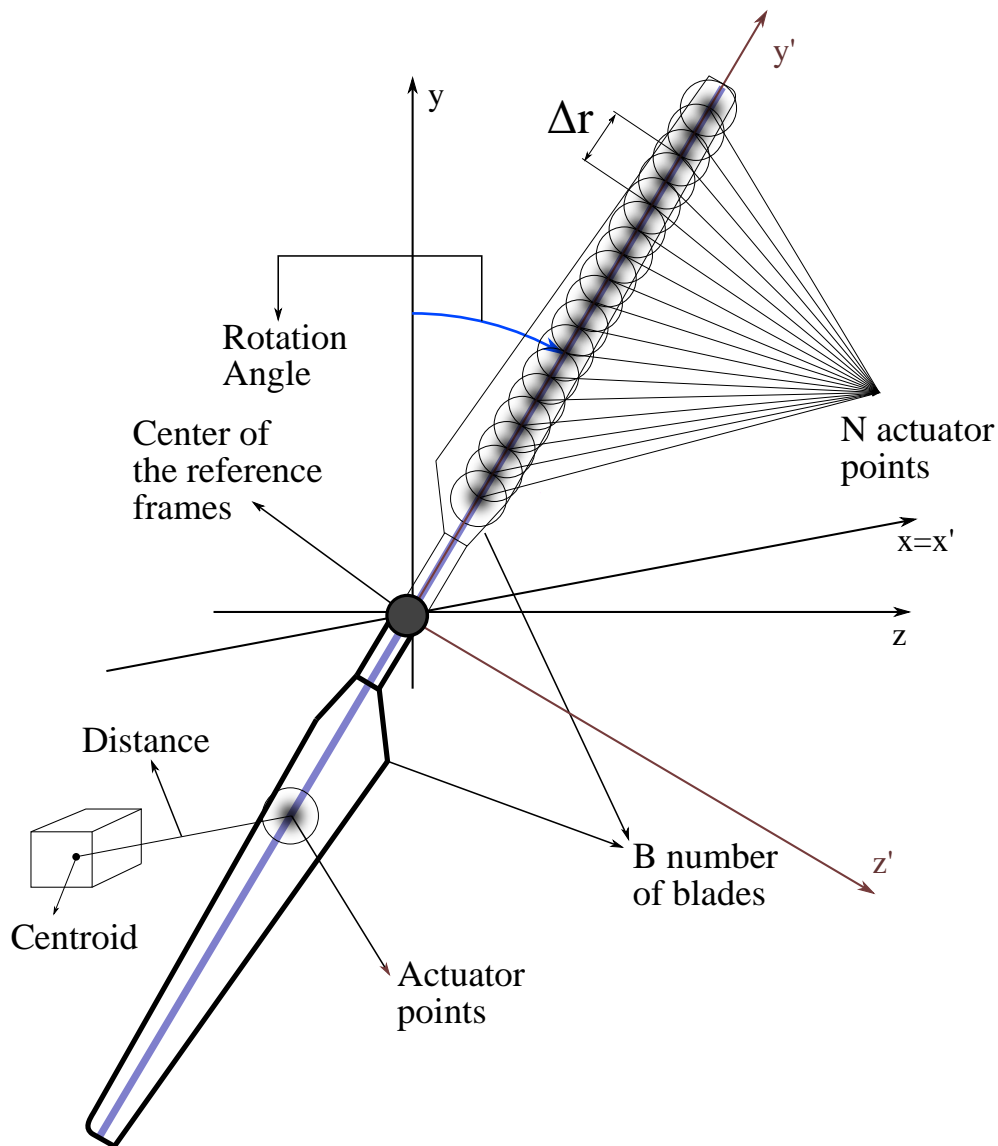
Figure 4.2: Representation of the main concept of the actuator line method. The rotor geometry is replaced by series of actuator points.

4.2 Parameters setup

As said in section 2.4, the ALM has some parameters to be set. Numerically the problem will be analysed in Chapter 5. Apart from geometrical and fluid dynamics/boundary conditions, the model is really sensitive to the regularization parameter ε of the kernel, to the number of actuator points and to the sphere radius of the Gaussian distribution R_s (see Figure 4.3). All those parameters have to be combined: this can be achieved through a sensitivity analysis (Chapter 5).
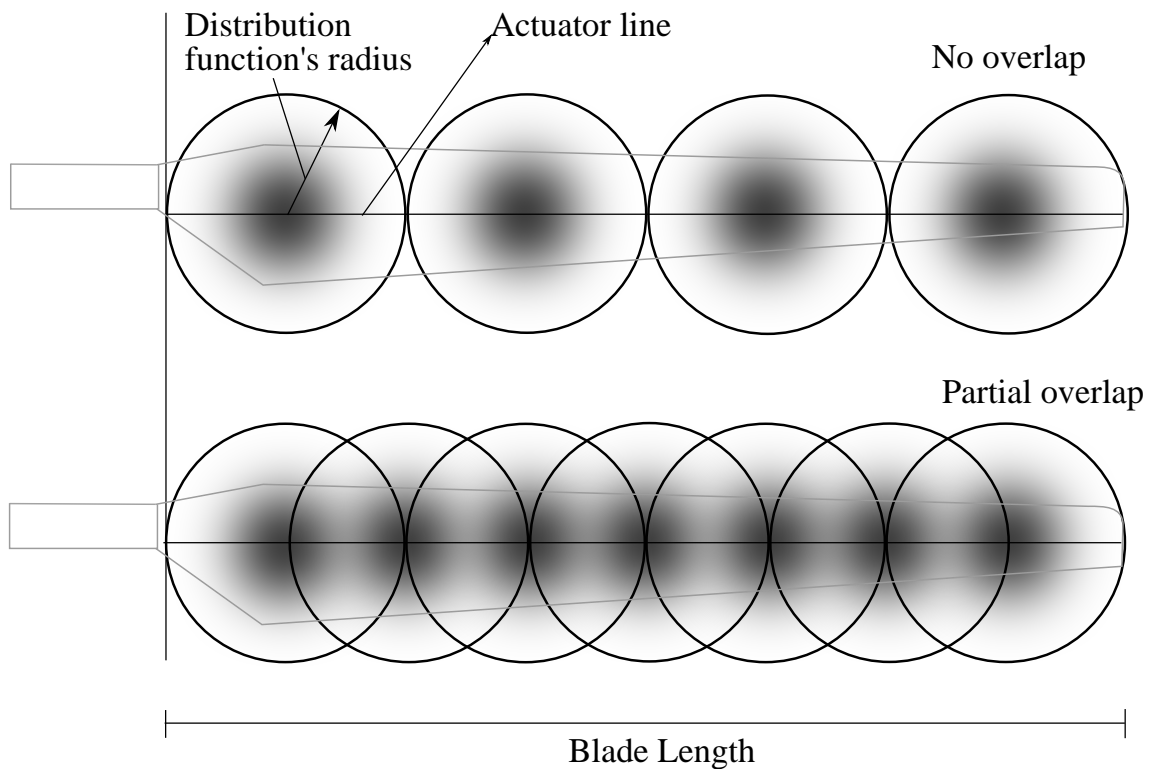
Figure 4.3: Representation of the typical parameter of the actuator line method. Each actuator point has an intensity determined by a Gaussian distribution, so decreasing from the center to the surface of the sphere.

To have set the ALM the following the steps has to be considered:

- The radius of the spheres of the distribution has to be set in the way that the volume occupied is almost the same of the blades. So, increasing the radius, the distribution becomes large which could lead to an overestimation of the inference between the turbine and the flow field. On the other hand, if the distribution radius is too small the software could encounter singularity problems or, if the distance between the actuator point and the centroid of the closest cell is higher, the source is omitted underestimating the turbine interference on the flow;

- For the purpose to have a continuous effect along the blade the overlapping between adjacent spheres are necessary. No overlap means a discontinuity between the actuator points, while a huge overlap leads to an increased computational cost, linked to a reduction of the cell size. A good compromise will be shown in the Section 5.4

So, as said in Section 2.4, the choice of the regularization parameter and of the radius of the sphere of distribution is crucial to have a stable and continuous effect in the turbine region and to have a good wake effect in the fluid domain.

CHAPTER 5

Sensitivity Setup

The main purpose of this chapter is to perform a sensitivity test of the model and to explain the parameters chosen for the simulation of this wind turbine. In fact, the parameters are machine-dependent. The main parameters to set up are the time step, the regularization parameter, and the sphere radius of the Gaussian force distribution, the cell volume and the boundary conditions.

To get a valid compromise between computational cost and accuracy the following parameters have been analysed:

- Dependency of the time step on the solution;

- Dependency on the grid;

- Influence of the regularization parameter ε ad the size of the sphere of distribution;

- Sensitivity at the boundary conditions.

The sensitivity analysis has been conducted by sampling the velocity, in function of time, into a line, located on the rotor plane, as shown in Figure 5.1.
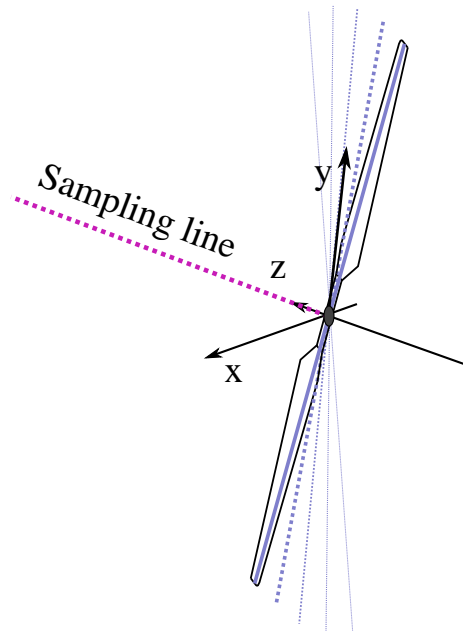

Figure 5.1: Sampling line.

The line starts from the center of the turbine and it is following the radial direction along the z-Coordinate of the inertial frame. So, sampling the data into several full rotation of the turbine

the radial time-averaged variables can be computed.

5.1   Time Step Sensitivity

The size of the time step define also the size of the rotation unity and it is critical for a stable solution.

The first parameter to check is the Courant number (CFL), which should be less than 1. If the Courant number is exceeding the angle increment of each step this means that the information contained in one cell of the fluid domain is flowing through more than one cell per time step, losing accuracy. The CFL is defined as:

$$CFL = \frac{U \Delta t}{\Delta x} \tag{5.1}$$

where Δx is the length of the cell in the flow direction [14]. It has been shown that at 7.016m/s and with a time step of 0.002s, as explained below, the CFL is not exceeding 0.055 in the smallest cells. So, the fluid domain looks to be in a safe condition.

Moreover, it is shown in [14] that the minimum number of time steps per one full rotor rotation should be greater than

$$N_{min} > 2\pi R / \Delta y \tag{5.2}$$

For this set up, N_{min} is 252 time step per rotor rotation since the Δy, the grid size in y direction, (see Figure 5.2) for the mesh introduced in 3.2 was set at 0.125m. This means that the last actuator point at the tip should move of a length less than the cell size [14] (Figure 5.2). In fact, a big time step combined with a small grid size would not lead to a reasonable solution since some cells would be skipped decreasing the accuracy, while a small time step leads to a greater computational cost.

Knowing N_{min}, the maximum time step size can be computed solving the following equation:

$$\Delta t_{max} = \frac{2\pi}{N_{min} \omega} \tag{5.3}$$

where 2π is the full rotation angle, N_{min} is the number of time steps for a full turbine rotation extracted in the Equation 5.2 and ω is the rotation speed of the turbine. The only unknown variable is Δt which can be computed and it is equal to 0.0033s. The rotation angle in the
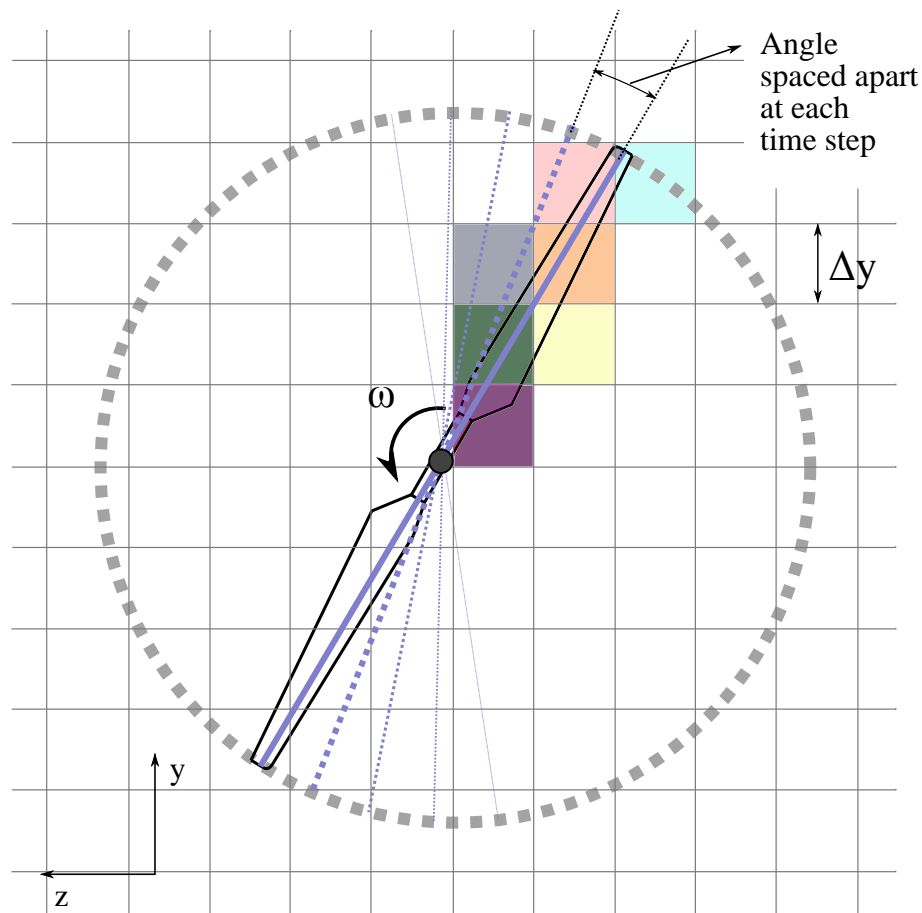
Figure 5.2: Coarse representation of the mesh structure and the maximum size of the respective time step.

current set up it is equal to 1.42 degrees for a rotation speed of 71.86 rpm. If the rotation speed is changing, time step has to be set again.

In Figures 5.3, 5.4 and 5.5, the results in the fluid domain subjected to different time steps size are represented. Referring to the Figure 5.3 the time step is too large and the forces are applied skipping some cells increasing the inaccuracy of the solution due to a discontinuity which brings the momentum forces not to be stable. Figures 5.4 and 5.5 correspond to a time smaller then time step found in Equation 5.2.

Obviously the solution is better in the last two cases, but smaller is the time step size, higher is the computational cost. A good time step has also been tested at 0.002s which will be used for all the CFD analysis.
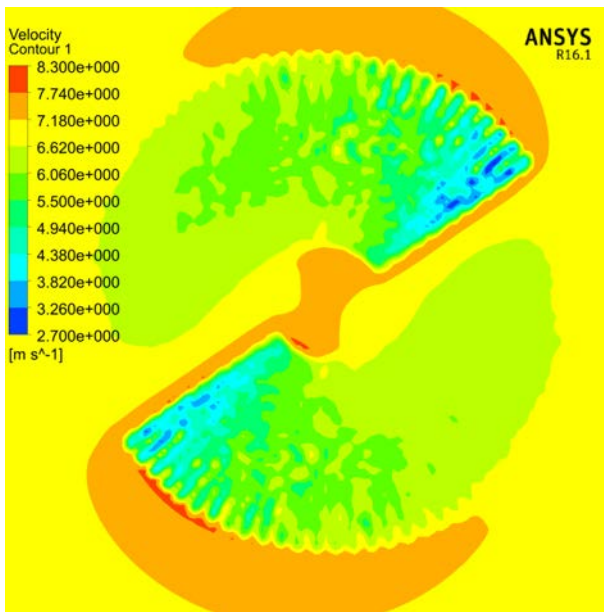
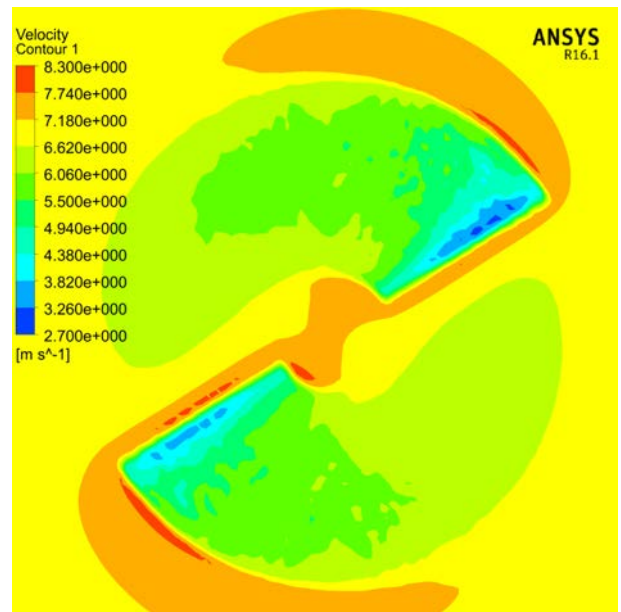**Figure 5.3:** Plot representation of the flow with a time step of 0.01.

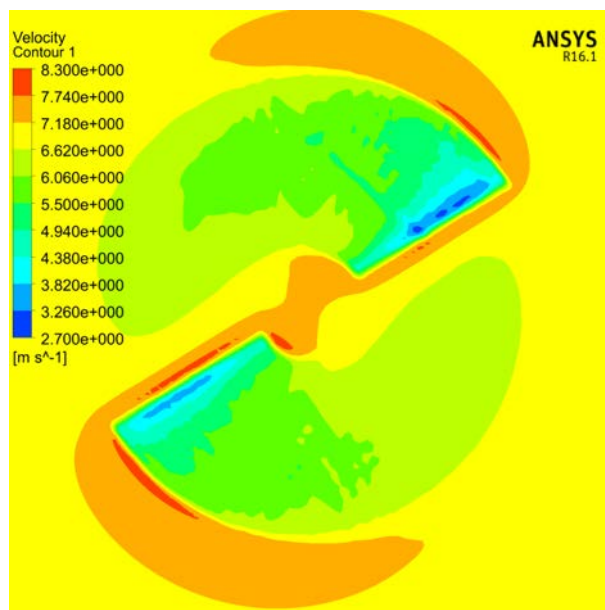**Figure 5.4:** Plot representation of the flow with a time step of 0.002.

Figure 5.5: Plot representation of the flow with a time step of 0.001.

This can be proved comparing the effect that the actuator points create on the fluid domain. In fact, for a small time step, Figure 5.6 compares, at x/R=0 (on the turbine), the results of time-averaged velocity for the three time steps considered and for three full turbine rotations. Moreover, it is clear that the large time step is less accurate because some cells are skipped,
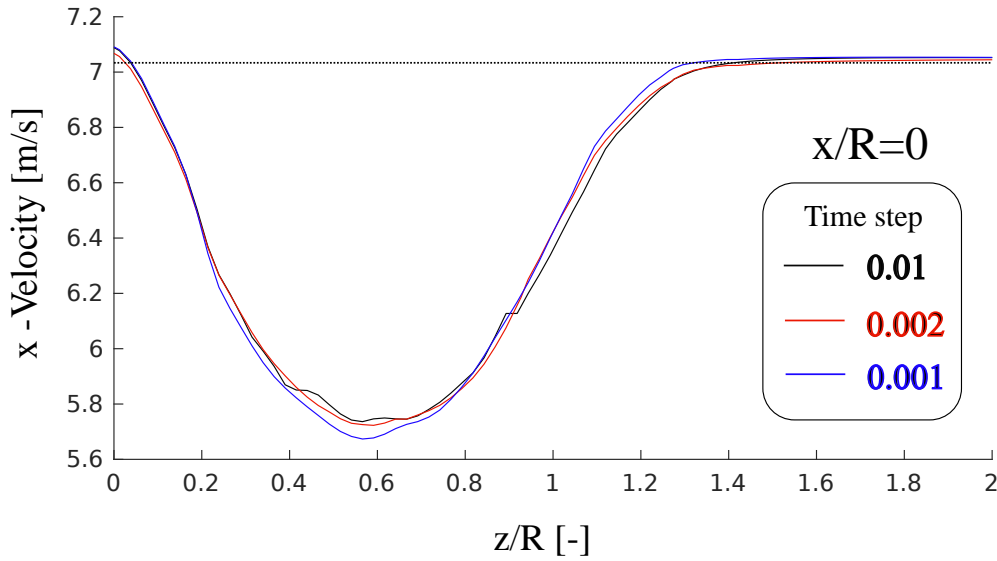
Figure 5.6: Representation of the x-Velocities in the fluid domain for the time steps of 0.01s, 0.0033s, 0.001s

while the small time step and the medium one have a similar effect. So a time step of 0.002 is a good compromise between the computational cost and the accuracy of the solution.

5.2 Kernel Sensitivity

In this section the influence of the Kernel $\mu_e(d)$ (Equation 2.66) is analysed. According to the volume size of the cells in the turbine region mesh (see Section 5.4), the parameter have to be set in order to smooth, to increase or to concentrate the forces applied in the fluid domain. So, the fluid domain is very sensitive to this value and the kernel has to be chosen properly. Different intensities of the kernel, parametric with epsilon, are shown in the Figure 5.7.

As said before, this parameter has the purpose to set the intensity of the input forces. So, different values of ε have been analysed and it has been demonstrated in the Chapter 6 that, for the mesh considered in the Section 3.2, the parameter ε set at 1.8 ensure a good correspondence between the velocities predicted by the BEM module and the velocities extracted from the fluid domain during the ALM simulation (see Section 6.2). In the Figure 5.8, it is possible to see the effect on the velocity extracted from the ALM domain, showing the dependency with the regularization parameter. A bigger regularization parameter is turning off the presence of the machine, while
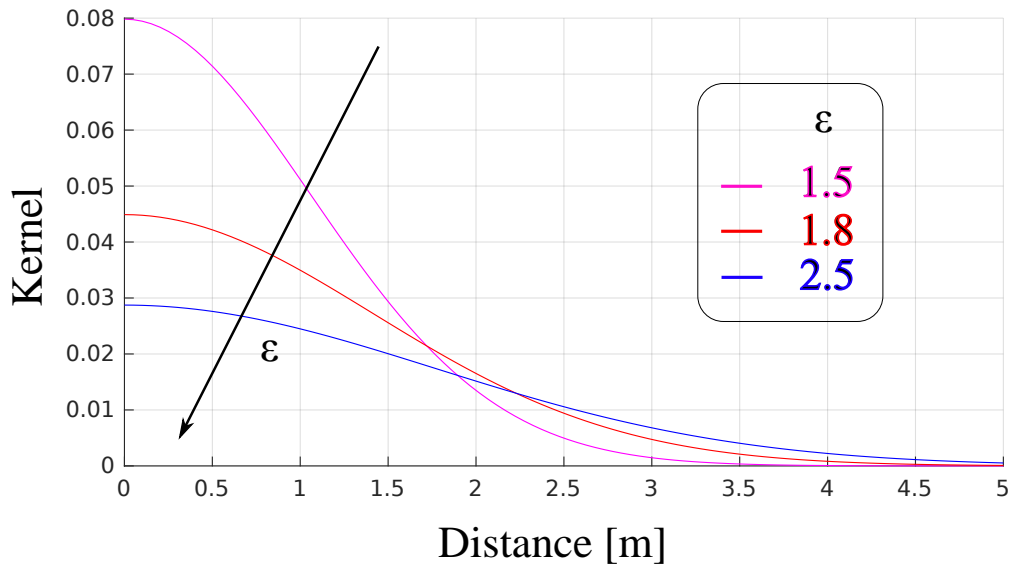
Figure 5.7: Graphical representation of the kernel for different regularization parameters.
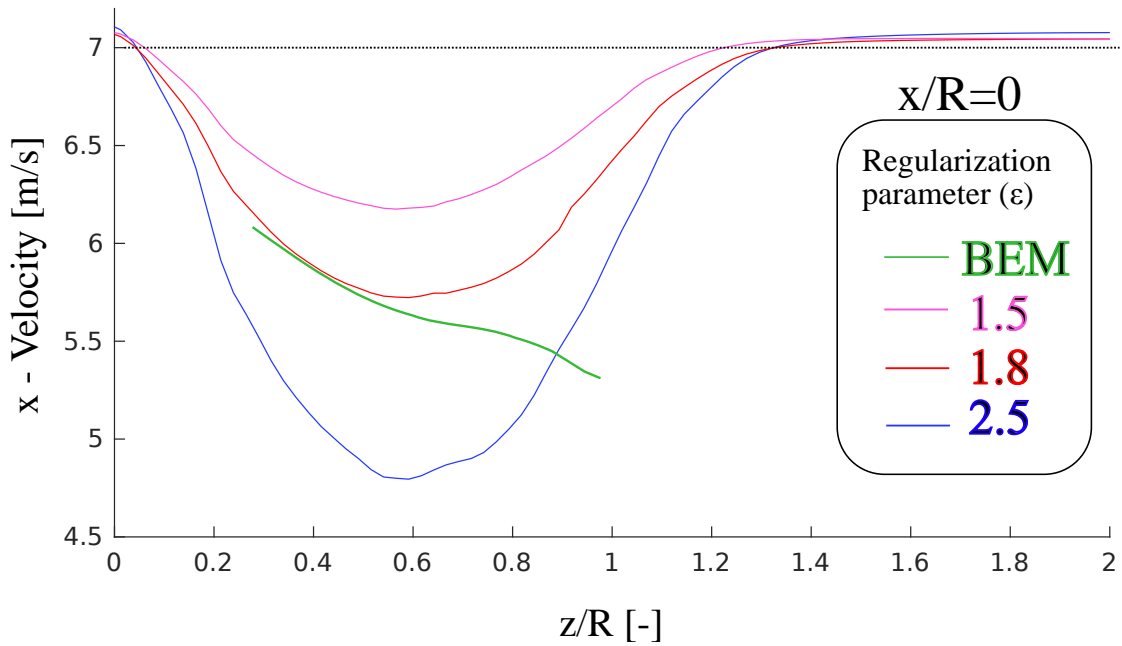

Figure 5.8: Results comparing the outputs of axial velocities for the three ε considered compared with the BEM ones.

a small ε is overestimating the forces increasing the blockage of the fluid domain.

5.3   Boundary conditions Sensitivity

First of all, the inlet and the outlet surfaces have to be located far enough in order to avoid non-physical behaviour in the fluid field. Secondly, symmetry conditions have been set for the lateral surfaces. An important check, moreover, is the distance of the turbine from the lateral boundaries. In fact, as it is shown in [14] the surfaces should be far enough to let the streamtube
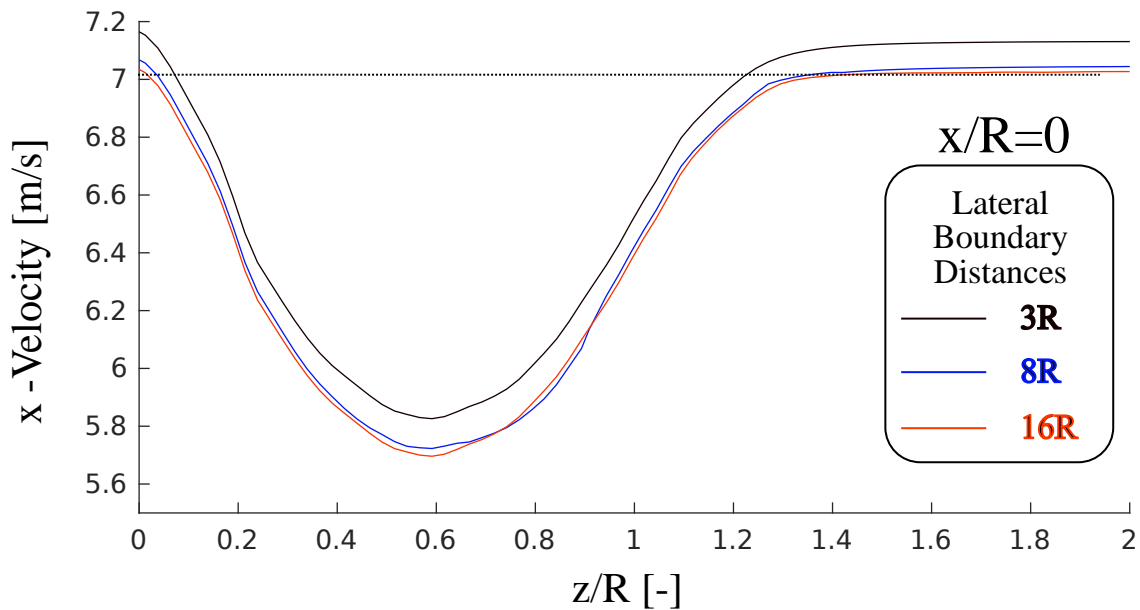

Figure 5.9: Representation of the averaged x-velocity along the radial direction for three lateral boundary distances.

to enlarge. Since the turbine is slowing down the fluid coming from the inlet creating a blockage, the flow streamlines distribute laterally. So, if the domain is too small to let the enlargement, the flow would accelerate around the turbine. It is possible to see this phenomena plotting the effect of the averaged x-Velocity along the radial line in the fluid domain (Figure 5.9)

5.4   Mesh Sensitivity

In this section the dependency on the computational domain is analysed. The effects and the consequences, the advantages and the drawbacks of a refined or coarse domain are studied. Moreover, the determination of the radius of the distribution sphere is explained, considering

the relationship with the mesh grid and the size of the blades in the turbine region. This check determines a good compromise among:

- The cell volume in the turbine region, so magnitude of the forces applied;

- The overlap of the spheres to avoid singularity problems and to guarantee the continuity from one actuator point to the next one. Moreover, the size of the distribution sphere has to be set in order to occupy approximately the same volume of the blades;

- The regularization parameter, which is set to diffuse the forces (see also Section 5.2).

First of all, the grid size is critical for the definition of the number of actuator points. In fact, they are chosen according to the grid cell size. It is a good compromise to set one actuator point for each cell encountered along the actuator line to have a smoother distribution of forces. For the grid considered 26 actuator points are enough to have the right discretization. The adopted
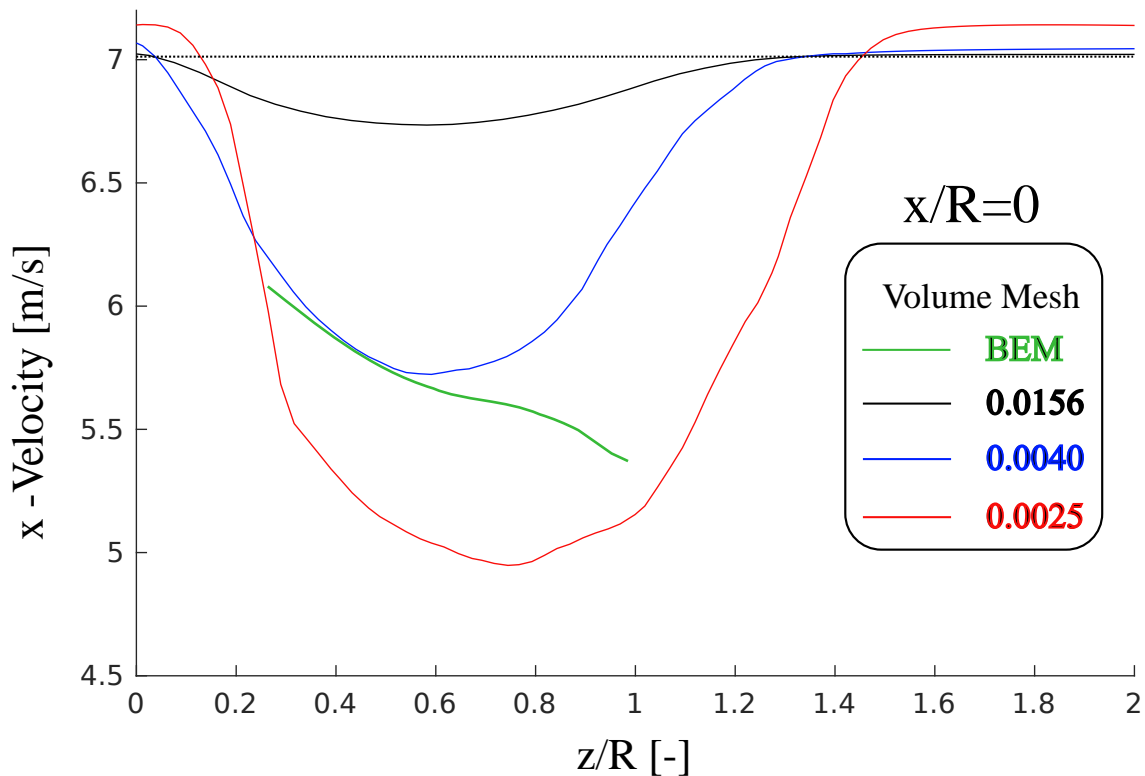

Figure 5.10: Results comparing the outputs of axial velocities for the three meshes compared with the BEM ones.

mesh has been analysed together with a coarser mesh and a refined mesh. Secondly, taking the distribution radius at three times the distance between two actuator points ($\simeq$0.3m), in order that the volume occupied by the spheres is approximately equal to the blade volume, a sensitivity test can be computed. The meshes analysed are reported in the Table 5.1.

Table 5.1: Features for the three cases setup.

Mesh	N cells	Δy [m]	$\Delta y/R_s$
Coarse	1700k	0.2546	0.70
Medium	4800k	0.1265	0.33
Refined	7000k	0.1010	0.27

The medium mesh coupled with 26 actuator points has been selected since, as in can be observed in Figure 5.10, the time-averaged axial velocity extracted from ALM calculations is similar to the trend of the axial velocity predicted by the BEM routine (see Section 6.2).

A radius of 3*Δr has been chosen for the sphere distributions, as a good compromise to avoid too much interference with the fluid domain and to guarantee the continuity from one actuator point to the next one. Moreover, since on the hub and on the tip region 3*Δr such a radius overestimates the local size of the blade, the script is compiled to consider only the centroids characterized by a radial distance from the center which is between R_{hub} and R_{tip}.

Validation Results

In this final chapter the results of a three step validation are illustrated. The first step is the validation of the standalone BEM routine against experimental data. The second step is the validation of the coupling between BEM routine, used as an initializer, and the ALM algorithm, which uses the forces computed by the BEM module. Finally the validation of the ALM against a CFD simulation of the full NREL Phase VI rotor is proposed. Contours of velocity and pressure are reported and commented.

6.1   BEM Validation

The first step is to validate the BEM routine using the experimental dataset of the NREL experiment [20]. This procedure ensures that this module of the code gives in output realistic results in terms of forces acting on the blade. Therefore a validation of the torque curve has been performed. Results are reported in Figure 6.1. A correct trend is observed, although a slight underestimation of torque is present for medium-high wind speeds.

Since all the analysis are computed with 7.016 m/sate BEM calculations are considered to be validated, thus the routine correctly predicts aerodynamic forces acting on the blades. This is fundamental since these forces are then used by the ALM algorithm to model the presence of the rotor. Moreover, the differences between the experimental data and the results from BEM are due to the inaccuracy in capturing the fluid behaviour in the stall region, reason why the rFoil tables have been used, as rFoil is more accurate in the stall region than xFoil [21].
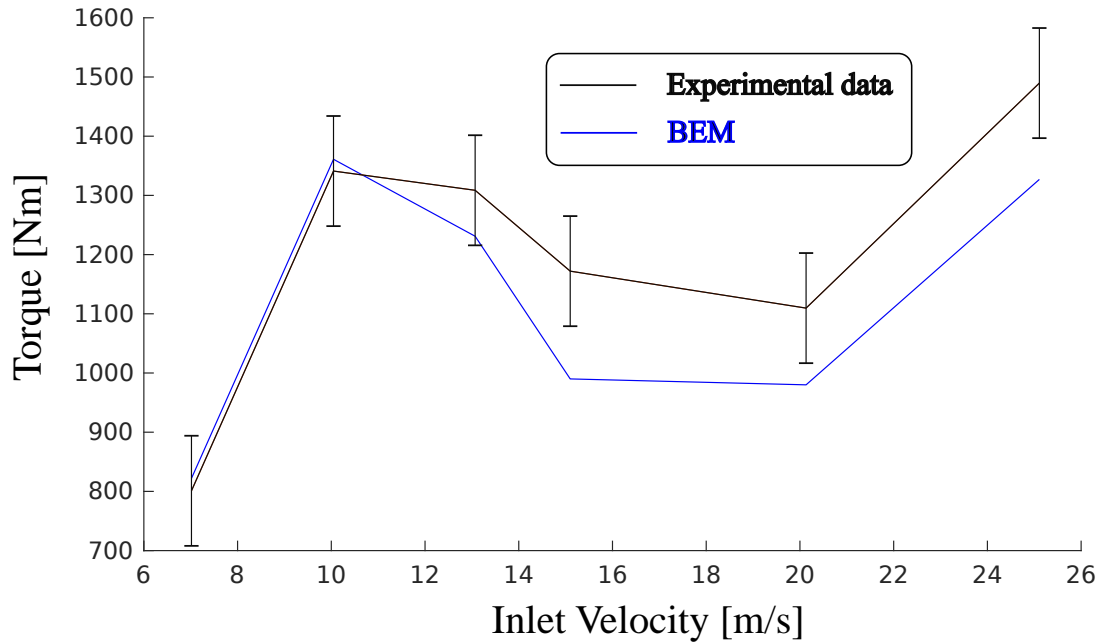
Figure 6.1: Representation of the analytical results of torque compared with the experimental data.

6.2   BEM-ALM coupling validation

Since the BEM routine demonstrated to give realistic results for the aerodynamic forces, this module of the code can be coupled to the ALM calculations, in order to give a proper value to the radial source terms. So the coupling of the BEM routine to the ALM algorithm has been validated in the following way:

- The BEM theory models the wind velocity reduction and deviation, due to the presence of the rotor, through the a and a' coefficients;

- The aerodynamic forces evaluated by the BEM routine are imposed to the fluid domain, in the ALM algorithm;

- If the fluid flow is slowed and deviated in a similar way to the BEM estimation, the effect of the actuator lines is considered to simulate the physical presence of the rotor.

Thus a validation on the axial and tangential induction factors is proposed. Values from ALM have been computed from the time-averaged values of velocities derived from three rotor revolutions.

The axial and the tangential induction factors are reported along the blades span in the Figures 6.2 and 6.3. The main differences between the numerical and the analytical a are due to the incapability of the analytical models to capture properly the fluid effects at the tip and at the hub. In fact BEM lacks to model the strongly 3D effects due to a finite blade length, turbulence, tip vortex and hub vortex. Therefore the numerical and analytical values of a differ in the outboard region of the blade, near the tip, whereas the tangential induction factor differs in the inboard region, near the hub. In the middle region of the blade instead values are correctly evaluated. Moreover, even though the a trend differs in the tip region, the analytical a values obtained from the BEM calculation are in good accordance with the one of [12]. About a', the general trend is respected, although a slight underestimation from the ALM.

Recalling the aim of this comparison, these results allow to confirm that the action of the rotating actuator lines in the ALM algorithm determine an effect of wind speed reduction and deviation in the flow field similar to the one predicted by the analytical calculation inside the BEM module. Therefore the BEM-ALM coupling is considered to be validated. The actuator line is ready to show some interesting results such as the stream-tube concept.

Figure 6.4 shows the trend of the axial induction factor computed from the time-averaged velocity along 4 lines set at 2m, 3m, 4m and 5m from the rotation axis parallel to the direction of the flow. Two important observations can be done:

- Moving from the upstream to the downstream, the axial induction factors increase, so the fluid is slowing down near the turbine decreasing the radius of the stream-tube in the upstream and enlarging it getting farther in the downstream;

- More the sampling line is close to the tip, less the induction factor is increasing. This phenomenon is due to a reduced blockage effect moving from the hub to the tip region.

In the downstream of the rotor it is clear that the fluid is influenced by the effect that the forces produce in the fluid domain since the axial induction factor has not a smooth trend as before the turbine.

Another variable extracted along the 4 lines just described is the static pressure gap of 3 full rotor revolutions. The Figure 6.5, in in accordance with the Figure 2.1, allows to observe one important fact. So, the pressure increases while approaching the turbine from the upstream, decreases in the downstream and go to the atmospheric pressure in the far-field.
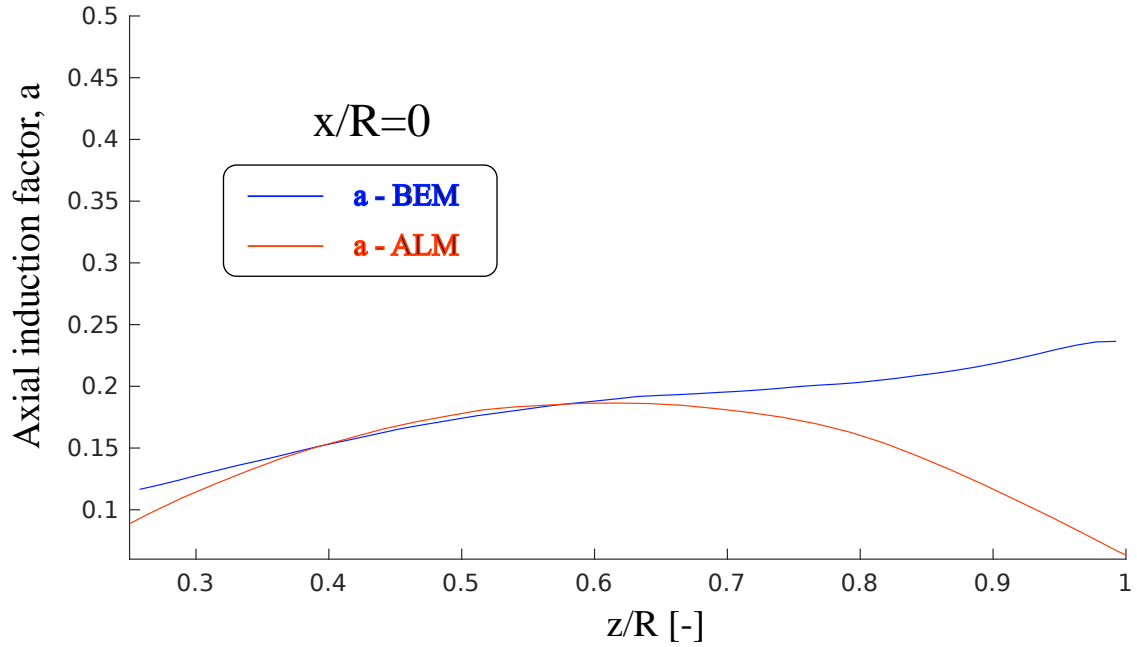
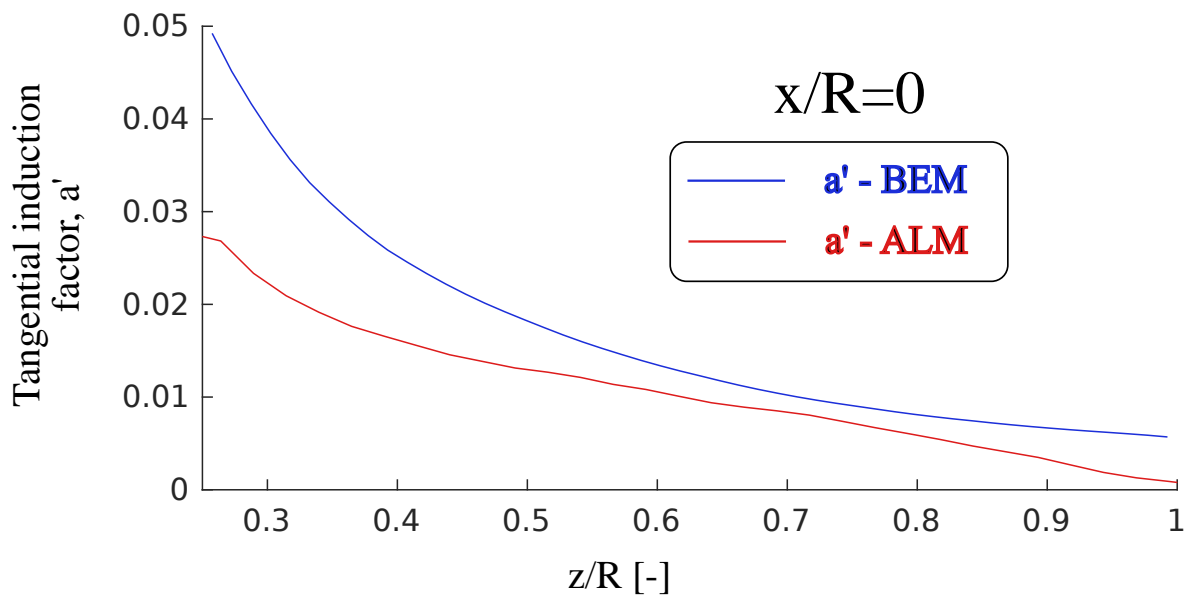**Figure 6.2:** Axial induction factors.

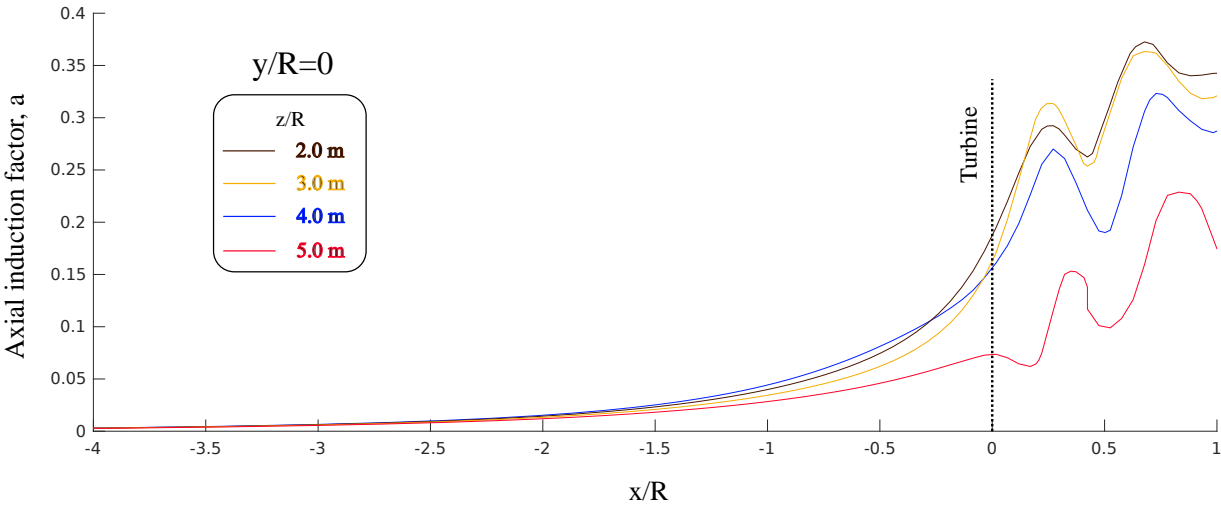**Figure 6.3:** Tangential induction factors.

Figure 6.4: Representation of the Axial induction factors along the axial direction.
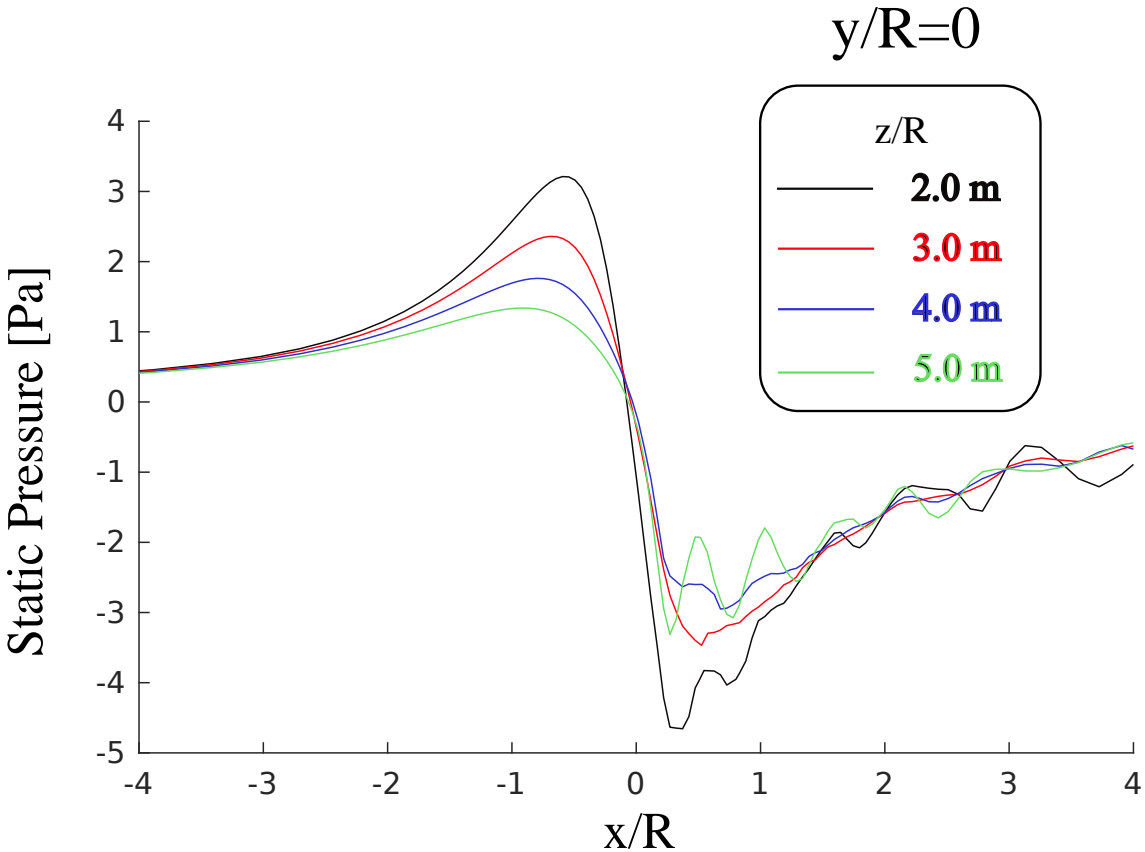

Figure 6.5: Representation of the pressure trend along 4 lines parallel to the fluid flow set ad different distances along the blade.

Figure 6.5 shows that the intensity of the pressure gap moving from 2 to 5 meters along the blade is decreasing, which shows that the 3D effects are influencing more the results getting closer to the tip.

6.3   ALM validation

The third and final step of the validation process deals with the validity of the ALM algorithm. The flow past the rotating actuator lines is compared to the wake computed by a CFD analysis of the full rotor of the NREL Phase VI, reported in [22], in terms of velocity and pressure contours. The CFD analysis performs a transient moving mesh calculation, applying the k-omega SST turbulence model performed. The wind velocity at the domain inlet is set to 10 m/s in both the simulations. The contours have been extracted after three complete rotor revolutions.

Five planes have been considered, downstream the wind turbine, to illustrate and compare the flow field predicted by the two approaches (ALM and CFD). The planes have been placed at different streamwise coordinate: x/R = 0.1, 0.25, 0.5, 1.0, 1.5 as shown in 6.6.
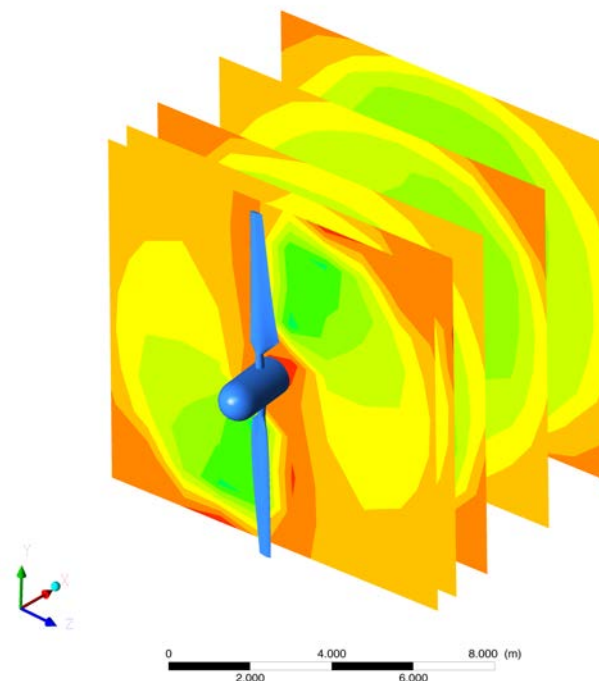

Figure 6.6: Planes employed for the contour analysis, placed at several x/R distances from the rotor plane.

The contour plots of the velocity field for the considered planes have been illustrated from Figure 6.7 to Figure 6.11. The first comparison has discussed the results in terms of velocity magnitude distributions. Both the ALM (on the left) and CFD (on the right) analyses have shown a good agreement in the determination of the wake behind the rotor. The shape of the wake is very similar in the two analyses and similar trends in its developing are observed. On the other hand, a slightly asymmetry is shown in the ALM wake prediction, where the CFD shows a proper symmetric behaviour. For all the considered planes an expansion discrepancy between the two numerical models occurred in radial and azimuthal directions. For a given plane, in radial direction, the wake predicted by the ALM code is slightly less extended then the CFD results, on the other hand, the expansion in the tangential direction is also slightly underestimated. Observing the trend of the flow field along the streamwise direction (x-direction) it can be noticed how the ALM seems to be more dissipative than the CFD approach, showing a velocity flow field of lower intensify in every considered plane. In the last plane (x/R=1.5) the velocity increases due to the blade tip effects is almost negligible, reaching the undisturbed value, where the CFD prediction still shows the development of the tip vortexes.
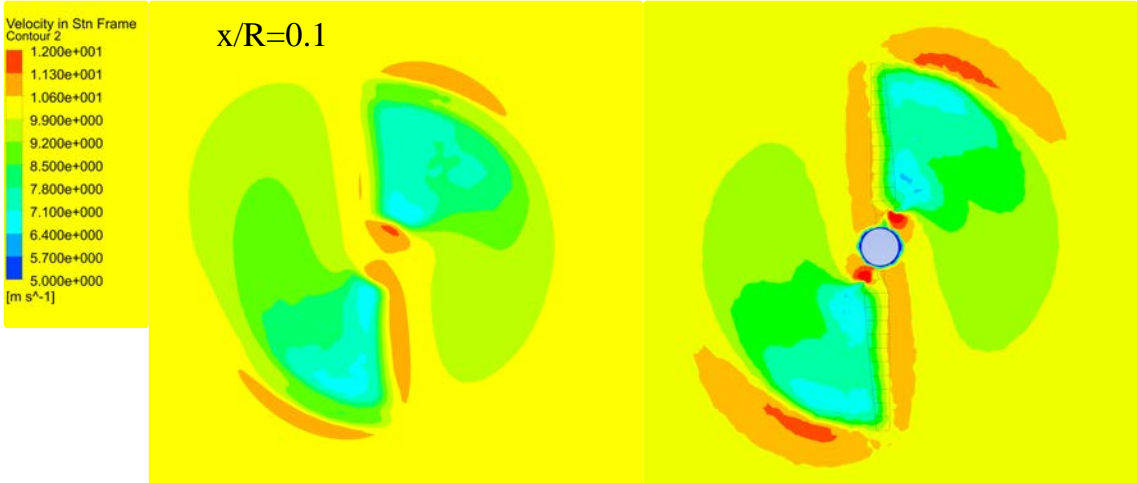
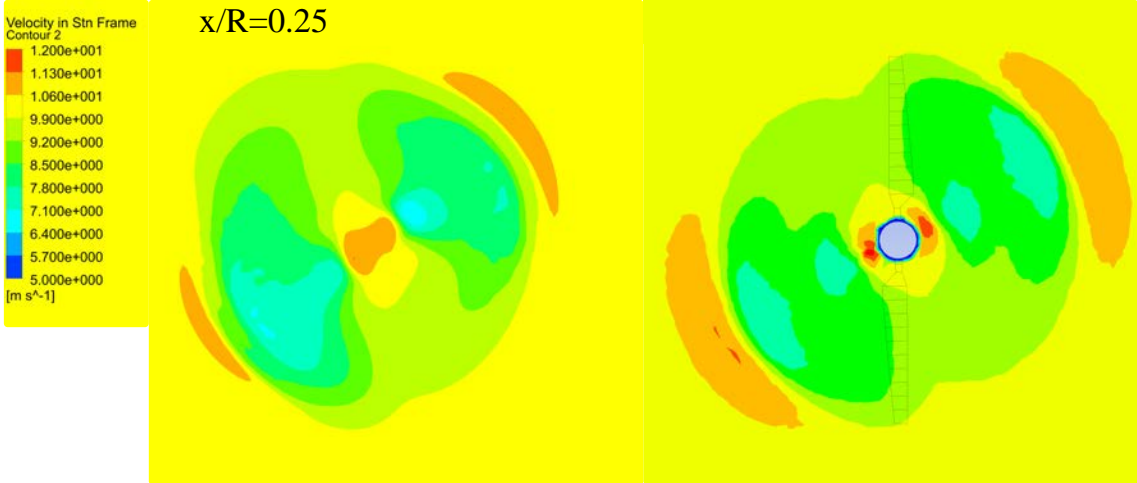**Figure 6.7:** Representation of the velocity at a distance of x/R=0.1.

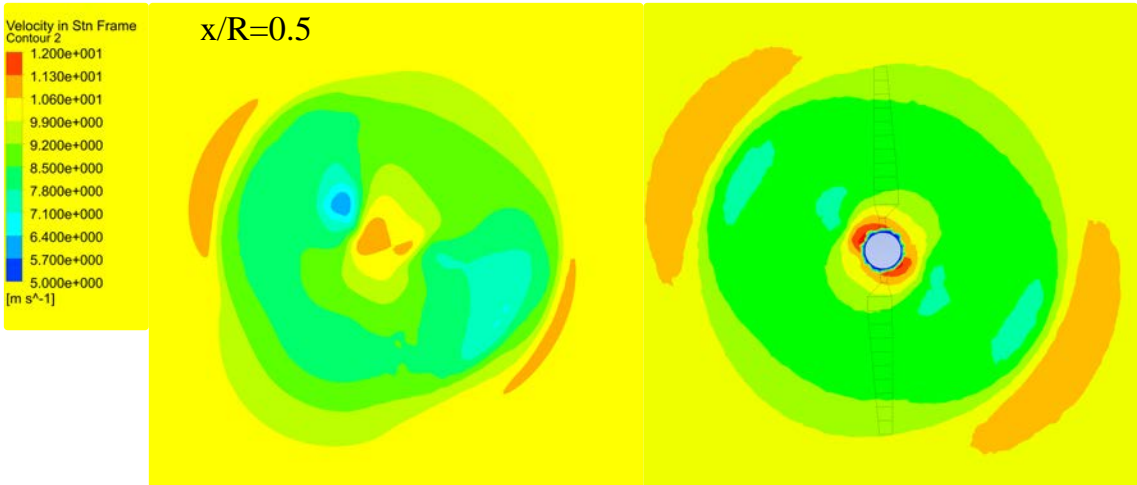**Figure 6.8:** Representation of the velocity at a distance of x/R=0.25.

Figure 6.9: Representation of the velocity at a distance of x/R=0.5.
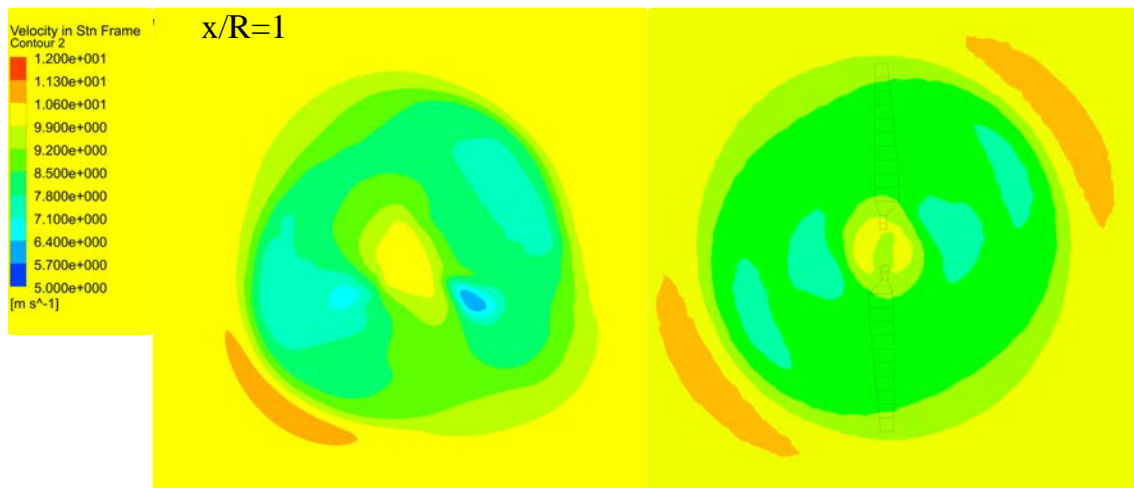
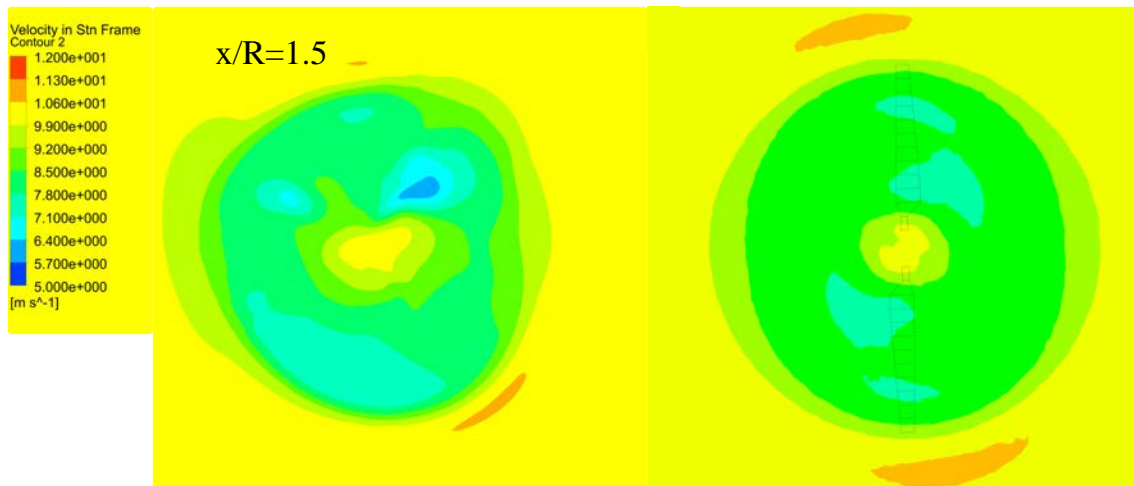**Figure 6.10:** Representation of the velocity at a distance of x/R=1.0.

Figure 6.11: Representation of the velocity at a distance of x/R=1.5.

The second comparison shows the flow field in terms of static pressure distribution. The contour plots of the static pressure field for the considered planes have been illustrated from Figure 6.11 to Figure 6.15. In the first plane (x/R=0.25) closest to the rotor the CFD better calculates the drop of pressure approaching the leading edge of the blade, where the ALM show a lower intensity of this drop. As observed for the velocity contour plots, the pressure flow fields show a good accordance between the two codes, furthermore the intensity of the predicted pressure is very similar in all the considered planes To conclude the ALM shows an overall similar behaviour than the CFD in predicting the development of the shape of the wake with slightly differences in determining the intensity of some flow field parameters; in particular, the velocity intensity results to be slightly underestimated.
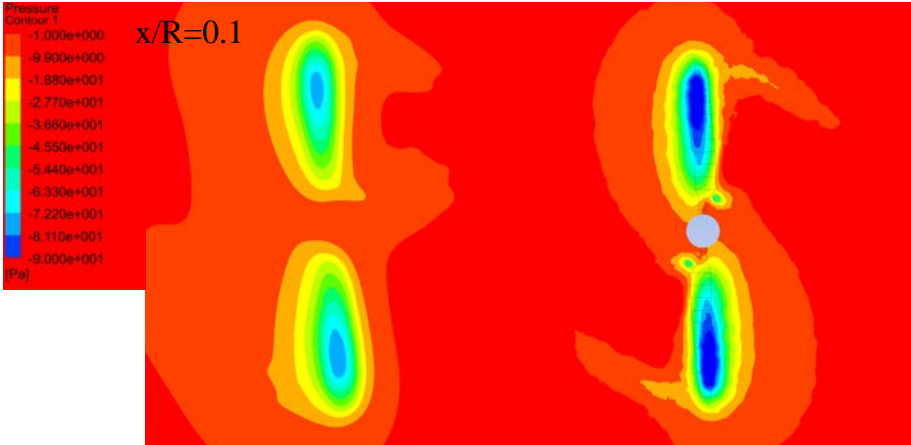
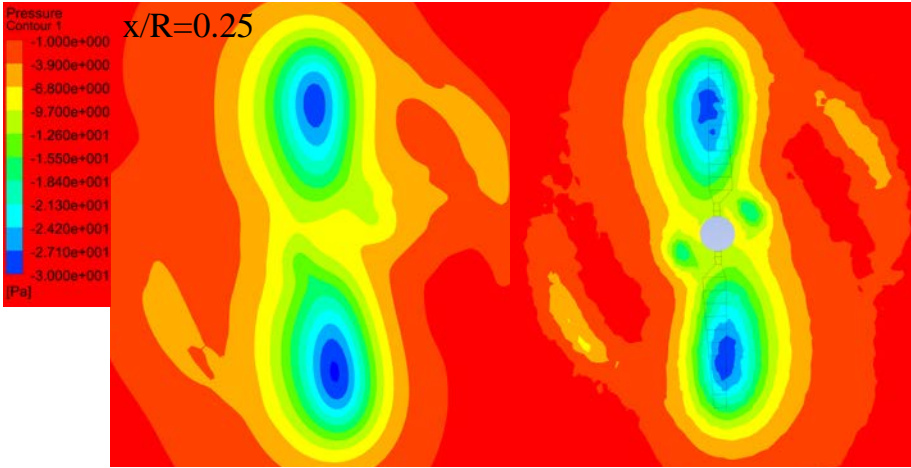**Figure 6.12:** Representation of the pressures at a distance of x/R=0.1.

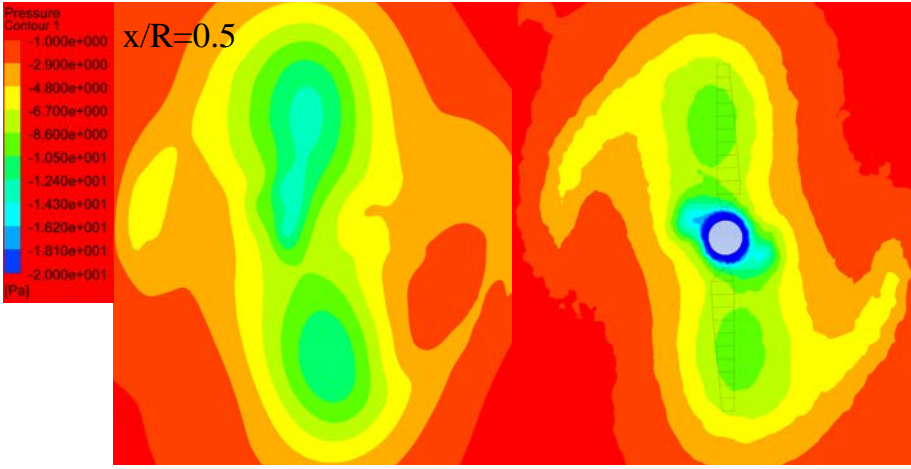**Figure 6.13:** Representation of the pressures at a distance of x/R=0.25.

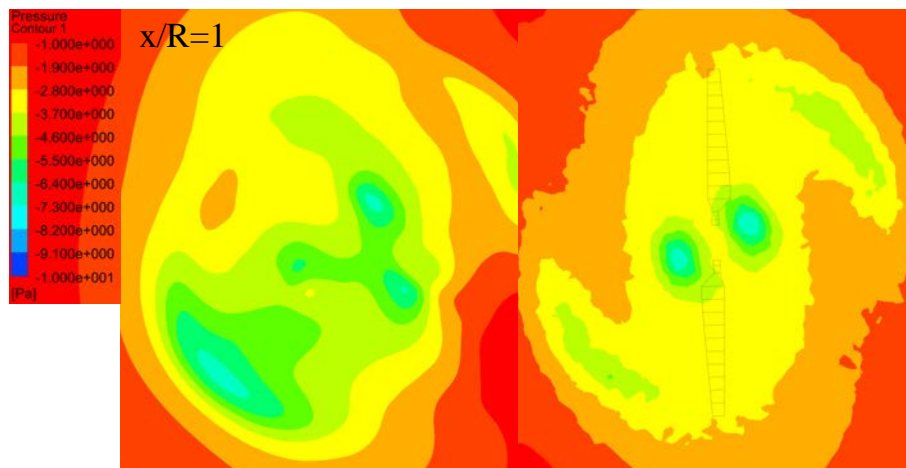**Figure 6.14:** Representation of the pressures at a distance of x/R=0.5.

Figure 6.15: Representation of the pressures at a distance of x/R=1.0.
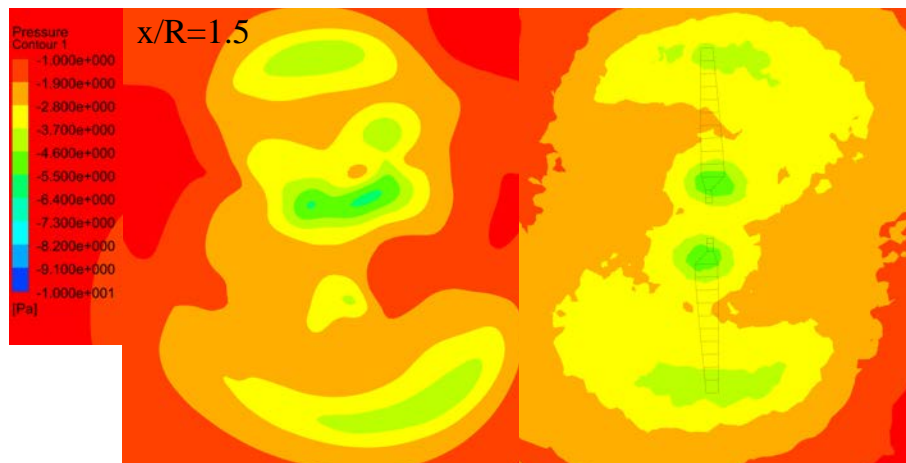

Figure 6.16: Representation of the pressures at a distance of x/R=1.5.

Figures 6.17 and 6.18 show and compare the development of the wake downwind the rotor, in the XZ plane, for the ALM and CFD analyses. As can be observed, the ALM predicts well the development of the shape of the wake with both a correct identification of the position of the tip vortexes and a comparable evaluation of the main structures of the wake. On the other hand, again, the ALM demonstrates to be more dissipative than the CFD analysis, underestimating the intensity of the velocity flow field in the wake. Furthermore, a difference is also observed in the streamtube evolution: the CFD predicts a streamtube expanding its size downstream, whereas the ALM does not. The different behaviour could be explained recalling the differences between the compared models: the ALM does not consider the presence of the nacelle and the connection parts between the first profile of the blade and the hub. By modelling these geometric features,

79

the CFD analysis is allowed to consider also the central vortex of the rotor; its presence radially expands the overall dimension of the wake.
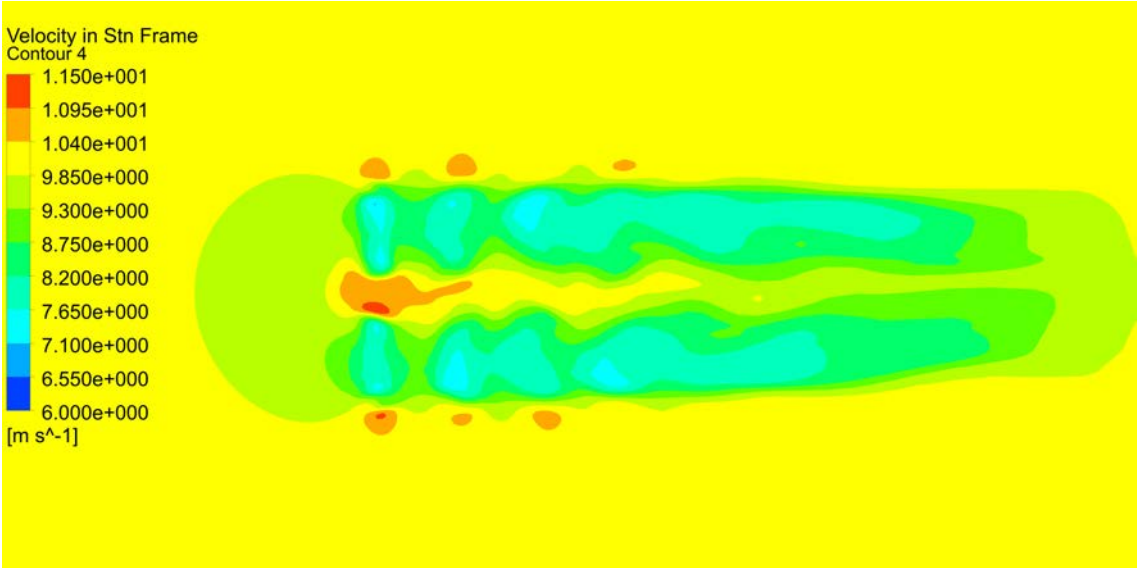

Figure 6.17: XZ view of the velocity contour, ALM analysis.
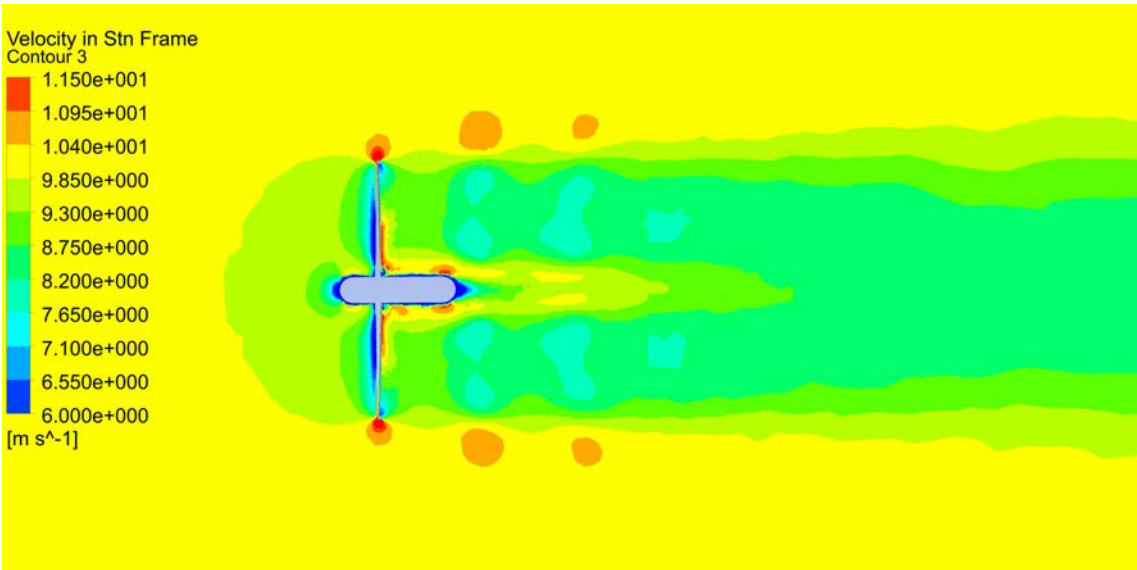
Figure 6.18: XZ view of the velocity contour, CFD analysis.

In Table 6.1 the size and computational time required by the two simulations are reported. Both the analyses have been run on 2 nodes composed by 32 intel(R) Xeon(R) cores with a clock core of 2.00GHz and 128GB of RAM memory.

Table 6.1: Comparison of features.

	ALM	CFD
N cells	4.8M	10M
CPU time	$\simeq 15H$	$\simeq 100H$

The lower computational cost required by the ALM is noticeable. This is the main advantage of the ALM methodology if compared to a full rotor CFD analysis.

CHAPTER 7

Conclusions

In this work, an Actuator Line Model (ALM) algorithm has been developed, by coupling Ansys Fluent to C-programming scripts. Moreover, also a Blade Element Method (BEM) routine has been implemented, in order to couple it to the ALM and grant a realistic initialization to the sources of the ALM. The parameters setup has been explained, and a good compromise between computational cost and accuracy of the solution has been reached.

A three-steps validation has been conducted, confirming the validity of the *BEM routine*, whose results have been compared to experimental data, the *BEM-ALM coupling*, which models the presence of a full rotor in the flow field and the *ALM algorithm*, whose results have been compared to a CFD of a full rotor.

The results obtained from the ALM code developed lead to the following statements:

- A BEM code alone is fast and predicts correctly the aerodynamic loads acting on the wind turbine. However, no information about the 3D flow field surrounding the wind turbine is available, i.e. an analysis on wake effects or a study on interference between more turbines cannot be done;

- A CFD of a full rotor grants information of the entire flow domain and a correct prediction of the machine performance. However such a simulation is linked to an increased computational effort, due to the 3D geometry, to the boundary layer and so to a more complex mesh characterized by an increased size;

- An ALM algorithm as the one developed in this work addresses both to the deficiencies of a BEM calculation and to the difficulties coming with a standard CFD analysis, combining the advantages of the two. In fact the main performance of the machine are correctly

83

predicted, since a BEM routine is adopted for the initialization of the ALM. Moreover, the 3D flow field is present and influenced from the actuator lines, which replace the 3D geometry of the rotor. So the discretization of the flow domain is easier, since no geometry and boundary layer have to be considered, with a reduced computational effort.

Future developments could be the application of such a methodology for the analysis of the interference between two wind turbines, and the study of turbines operating in extreme wind conditions. Another application could be the preliminary analysis of complex systems, for example floating wind turbines behaviour. In fact, such a configuration would be of utmost difficulty to be modelled with a standard CFD, whereas a BEM analysis alone would be over-simplified. On the other hand, the application of such an ALM algorithm can deal with the movements of the system while keeping a simple mesh, giving in output reliable pressure contours and force trends.

References

[1] Wind in power 2017. Annual combined onshore and offshore wind energy statistics; February 2018. https://windeurope.org/about-wind/statistics/european/wind-in-power-2017.

[2] *International Energy Agency*, Renewables information. www.iea.org.

[3] G. Pavesi. *University of Padua*. Professor's notes; 2016-2017.

[4] Christofer Hung, Dirk Schindler, Jessica Laible; *National and global wind resources assessment under six wind turbine installation scenario*; Energy Conversion and Management 156 (2018) 403-415.

[5] *Aerodynamics of Wind Turbines*, Martin O. L. Hansen, 2008; Chapter 1,2-3;

[6] 9 dic 2013; http://centurionenergy.net/types-of-wind-turbines.

[7] Madjid Karimirad, *Offshore Energy Structures for Wind Power, Wave Energy and Hybrid Marine Platforms*. Chapter 2: pag 7-21, 2014.

[8] *ANSYS FLUENT 16.1 Theory Guide* 2-3.

[9] *Aerodynamics of Wind Turbines*, Martin O. L. Hansen, 2008, Chapter 6;

[10] Joachim Peinke, University of Oldenburg, Oldenburg, Germany; *General Momentum Theory for Horizontal Axis Wind Turbines*, Chapter 3, 10-11, 2016, forth edition;

[11] *Aerodynamics of Wind Turbines*, Martin O. L. Hansen, 2008; Chapter 6;

[12] Wen Zhong Shen *Tip Loss Correction for Actuator/Navier–Stokes Computations*, Department of Mechanical Engineering, Technical University of Denmark, DK-2800 Lyngby, Denmark.

[13] Wen Zhong Shen, Robert Mikkelsen and Jens Nørkær Sørensen *Tip Loss Corrections for Wind Turbine Computations*, Department of Mechanical Engineering, Technical University of Denmark, DK-2800 Lyngby, Denmark.

[14] Troldborg, Niels; Sørensen, Jens Nørkær; Mikkelsen, Robert Flemming, *Actuator Line Modeling of Wind Turbine Wakes*, Technical University of Denmark, 2009

[15] P. Giguère and M.S. Selig, *Design of a Tapered and Twisted Blade for the NREL Combined Experiment Rotor*, NREL/SR-500-26173, April 1999.

[16] *ANSYS FLUENT 16.1 Theory Guide* 56-57.

[17] *ANSYS FLUENT 16.1 Theory Guide* 46-47.

[18] *ANSYS FLUENT 16.1 Theory Guide* 644-647.

[19] *ANSYS FLUENT 16.1 Theory Guide* 632-633.

[20] D. Simms, S. Schreck, M. Hand, L.J. Fingersh, *NREL Unsteady Aerodynamics Experiment in the NASA-Ames Wind Tunnel: A Comparison of Predictions to Measurements*, National Renewable Energy Laboratory.

[21] Giridhar Ramanujam, Huseyin Ozdemir H.W.M.Hoeijmakers *Improving Airfoil Drag Prediction*, 4-8 January 2016, San Diego, California, USA, 34th Wind Energy Symposium.

[22] L. Menegozzo, A. Dal Monte, E. Benini, A. Benato, *Small wind turbines: A numerical study for aerodynamic performance assessment under gust conditions*, Department of Industrial Engineering, University of Padua, Via Venezia 1, Padua, Italy, Renewable Energy 121 (2018) 123-132.